

Experimental investigation on the power capture of an oscillating wave surge converter in unidirectional waves

Moisés Brito ^{a,*}, Rui M.L. Ferreira ^a, Luis Teixeira ^b, Maria G. Neves ^c, Ricardo B. Canelas ^a

^a CERIS, Instituto Superior Técnico, Universidade de Lisboa, Av. Rovisco Pais, 1049-001, Lisboa, Portugal

^b Instituto de Mecánica de los Fluidos e Ingeniería Ambiental (IMFIA), Facultad de Ingeniería, Universidad de la República, 11200, Montevideo, Uruguay

^c Harbours and Maritime Structures Division, Hydraulics and Environment Department, Laboratório Nacional de Engenharia Civil (LNEC), Av. do Brasil 101, 1700-066, Lisboa, Portugal



ARTICLE INFO

Article history:

Received 18 June 2018

Received in revised form

8 October 2019

Accepted 17 November 2019

Available online 22 November 2019

Keywords:

Wave energy

Oscillating wave surge converter: OWSC

Capture width ratio: CWR

Response amplitude operator: RAO

Power take-off: PTO damping

ABSTRACT

The aim of this paper is the experimental characterization of the capture width ratio (CWR) and response amplitude operator (RAO) of a 1:10 physical model of an oscillating wave surge converter (OWSC), under unidirectional regular and irregular waves. The effects of hydraulic power take-off (PTO) system are explicitly taken in consideration. A mathematical model is proposed to describe the PTO damping as a function of the angular velocity of the flap. The harmonic decomposition of free-surface elevation, angular velocity of the flap and pressure in the PTO system demonstrates that these signals are dominated by their linear component. However, the signals also present some important higher-order frequency components. To predict the CWR of the OWSC under irregular waves the nonlinear output frequency response functions are considered as the extension of the RAO to the nonlinear case. It is shown and discussed that the PTO system, wave frequency and height have a significant influence on the CWR and RAO. The RAO curve for irregular waves does not exhibit a well-defined peak, showing a limited variation in a broadband. A weak correlation between CWR and RAO was found, i.e., the maximum CWR does not occur for the maximum value of RAO.

© 2019 Elsevier Ltd. All rights reserved.

1. Introduction

Oscillating wave surge converters (OWSCs) are an important class of oscillating wave energy converter (WEC) devices, designed to operate in the nearshore region, i.e., with water depth ranging between 10 and 20 m [1]. OWSCs are composed of a buoyant flap and a hydraulic power take-off (PTO) system. The flap is usually attached to the foundation via bearings, presenting vertical position (fully or partially submerged) in the absence of waves and pitching under the action of incoming waves. The PTO system is composed of hydraulic cylinders and a closed hydraulic circuit. Therefore, OWSCs present at least three stages of energy conversion [2]. In the first stage the flap is excited by the wave, transforming the wave energy into mechanical energy, while in the second stage, the PTO system transforming the mechanical energy into potential energy. Finally, in the third stage the high-pressured fluid drives a hydraulic motor which converts potential energy into electrical

energy [1,3–5].

A comprehensive knowledge of the wave-flap and flap-PTO interactions in these stages of energy conversion is essential in the design and performance of OWSCs. However, due to the complexity of these interactions, most of previous works on the OWSCs had looked at the design and performance of the flap in laboratory-scale tests without hydraulic PTO system. Nevertheless, in analytical (see e.g. Refs. [6–12], and numerical studies (see e.g. Refs. [5,13–17], the PTO system is simplified and is often modelled as a linear damper.

Analytical studies of OWSCs were usually performed using linear wave theory. The solutions lead to important expressions for the hydrodynamic characteristics of the flap (e.g., added moment of inertia, radiation damping, wave excitation torque, mean power and capture width ratio (CWR)). However, in many cases, these solutions are not accurate enough to describe the complex hydrodynamics of OWSCs observed in the experimental studies [10,18]. Furthermore, the small amplitude regular waves considered by linear wave theory are not accurate for the power capture estimation in highly energetic seas, as the results cannot be safely extrapolated beyond the limits of linear theory [15].

At present, few experimental studies have been performed on

* Corresponding author.

E-mail address: moises.brito@tecnico.ulisboa.pt (M. Brito).

the dynamics of the OWSCs (see e.g., Refs. [2,3,19–23]. These studies have been focused on the effects of water depth, wave period and height, density, moment of inertia and location of centre of mass of the flap on the OWSC dynamics. Their results provide useful information but are still limited in what concerns the influence of hydraulic PTO system on the CWR and response amplitude operator (RAO) [24].

The aim of this paper is to present an experimental investigation on the CWR and RAO of an OWSC with hydraulic PTO system under unidirectional waves. For this purpose, the free-surface elevation, pressure in the PTO system and the rotation angle of the flap of an OWSC at 1:10 scale model were measured. The measurements were performed for both regular and irregular waves with the highest annual frequency, i.e., major contributors to the mean annual energy, in the Uruguayan oceanic coast [25].

The paper first presents the experimental results of an OWSC under regular waves, from which the CWR and RAO are obtained. The effects of PTO system, wave frequency and height on the OWSC dynamics are presented and discussed. The effects of nonlinearity due to large amplitude of flap motion are discussed. The experimental results are also used to develop a mathematical model of PTO damping as a function of the angular velocity of the flap. Then the experimental results of OWSC under irregular waves are analysed. Due to the nonlinearities, the RAO is analysed by harmonic decomposition. Finally, the nonlinear output frequency response functions are considered as the extension of the RAO to the nonlinear case to predict the CWR under irregular waves.

The novel contribution of this paper is an original experimental characterization of the CWR and RAO of an OWSC with hydraulic PTO system. This paper presents both linear and nonlinear analyses of OWSC under unidirectional regular and irregular waves. A mathematical model to describe the damping of hydraulic PTO system as a function of the angular velocity of the flap is proposed. A new analysis to predict the CWR of OWSCs under irregular waves based on RAO and nonlinear output frequency response functions is presented.

2. Experimental test

2.1. Physical model

The experimental tests were conducted in a horizontal wave flume at the Instituto de Mecánica de los Fluidos e Ingeniería Ambiental (IMFIA), Universidad de la República, Uruguay. The wave flume is approximately 60 m long (wave direction), 1.5 m wide and 1.8 m deep, and is equipped with a piston-type wavemaker. This wavemaker was controlled by AwaSys 6 [26], which can generate regular and irregular waves with active wave absorption of reflected waves. At end of the wave flume, there is a passive absorption beach with longitudinal slope of 0.3 m/m. The schematic sketch (side and plan views) of the experimental setup is shown in Fig. 1.

The OWSC model was positioned on the central line of the wave flume at a distance of 32.7 m from the wavemaker. The buoyant flap is composed by seven PVC tubes, stainless steel frame and bearings and is hinged on y -axis at 0.10 m above the flume bed. The main characteristics of the flap are given in Table 1. These characteristics were determined based on the OWSC model presented in Ref. [18]; for a relative density of about 0.4. Ref. [18] has shown that the changing of the flap's relative density from 0.3 to 0.5 have a little effect on the hydrodynamics and performance of the OWSCs for a large range of the incident wave periods.

The PTO system is composed of a hydraulic cylinder and a closed hydraulic circuit, which includes check-valves, globe valves, plastic tubes and reservoir (see Figs. 2 and 3). The check-valves prevent the non-return flow and globe valves allow the control of the flow rate and consequently the change of the coefficient of pressure loss (see Sec. 3). The hydraulic cylinder is linked to the flap at $z = 0.47$ m and $x = 0.09$ m, and to the flume bed at $z = 0$ and $x = 1.04$ m. In these experimental tests, the hydraulic cylinder was working as a single piston effect, with the upper cylinder chamber working at atmosphere pressure, P_{atm} . Fig. 2 shows the OWSC model.

Fig. 3 shows the schematic sketch (side view) of the OWSC model.

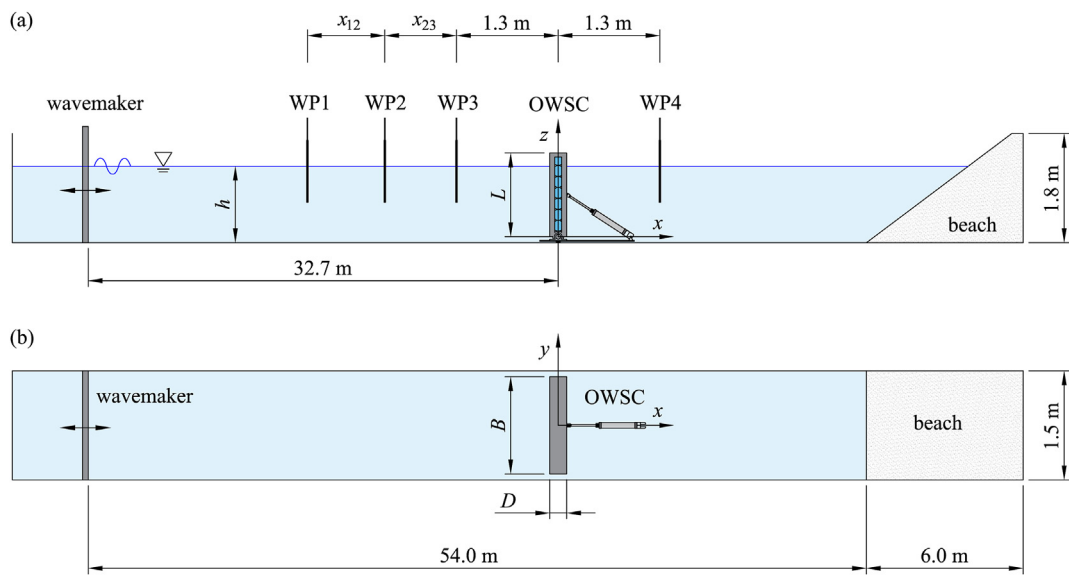
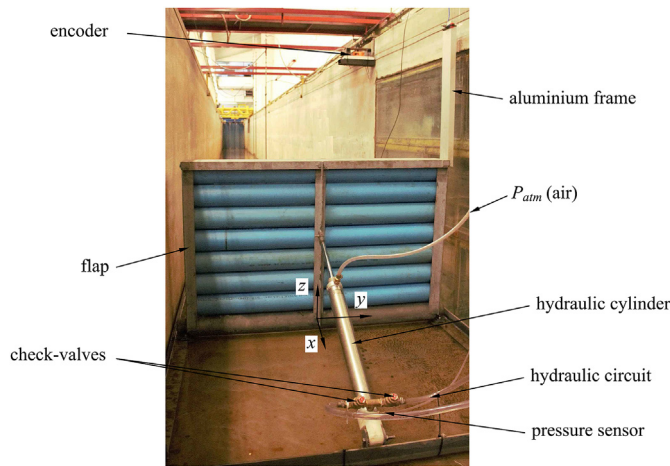


Fig. 1. Schematic sketch of the experimental setup (not to scale): (a) side view; (b) plan view.

Table 1

Dimension, mass and moment of inertia (about the bearings) of the flap.

Dimensions	Symbol	Value	Units
Height	<i>L</i>	0.84	m
Width	<i>B</i>	1.31	m
Thickness	<i>D</i>	0.17	m
Mass	<i>m</i>	72.3	kg
Moment of inertia	(<i>I_{xx}</i> ; <i>I_{yy}</i> ; <i>I_{zz}</i>)	(27.61; 14.76; 13.11)	kg m ²
Centre of mass	(<i>x̄</i> ; <i>ȳ</i> ; <i>z̄</i>)	(0; 0; 0.33)	m

**Fig. 2.** OWSC model.

2.2. Test conditions

In this paper, two set of experimental tests are presented, both using Froude's scale, with a geometrical scale factor $\lambda = 10$. Therefore, parameters such as wave height and water depth is linearly scaled as λ^{-1} , wave period and velocities as $\lambda^{-0.5}$ and power capture as $\lambda^{-3.5}$ [27,28]. Using Froude scaling has some limitations, due to neglect the viscous effects. However, the damping due to viscous drag at model scale is expected to be greater than at prototype scale, as the Reynolds number is lower [29].

The first set of experimental tests were carried out for regular

waves with still water depth $h = 0.825$ m. The wave condition considered comprises plane progressive waves of steepnesses ranging from $kH = 0.086$ to 0.385 and water depth ratios varying from $kh = 0.472$ to 1.058 , where h is the water depth as mentioned above, k and H denote the wave number and wave height, respectively. These conditions correspond to the predominant waves (those with the highest annual frequency, i.e., major contributors to the mean annual energy) in the Uruguayan oceanic coast [25]. According to the diagram by Ref. [30] the experimental wave conditions are in the range of validity of Cnoidal, Stokes 2nd and 3rd order wave model. Table 2 shows the wave conditions used for the regular wave tests, where T is the wave period and L is the wave length.

The second set of experimental tests were carried out for irregular waves with $h = 0.825$ m. Four groups (I1, I2, I3 and I4) of the incident unidirectional irregular waves generated by different wavemaker input signals were considered. Table 3 shows the characteristics of each wave condition, where T_p is the peak period, H_s is the significant wave height, H_m is the mean wave height, T_e is the energy period, T_m is the mean spectral period, T_z is the zero-crossing period, T_c is the crest period and P_w is the power per unit wave crest. Tests I1 and I2 correspond to two standard JONSWAP (Joint North Sea Wave Observation Project) spectrum, both with peak enhancement factor $\gamma = 1.2$ and tests I3 and I4 correspond to two field spectrum based on data measured at the Uruguayan oceanic coast [25].

The wavemaker was programmed to generate irregular waves defined by a spectrum. JONSWAP spectrum (tests I1 and I2) were directly selected on the AwaSys 6 interface and the field spectrum (tests I3 and I4) were read from external text files. I3 represents the maximum (in the peak frequency) and I4 represents the mean energy spectral density in the Uruguayan oceanic coast. The input spectrum, S_w , of each test is shown in Fig. 4.

2.3. Data acquisition and analysis

The rotation angle of the flap, θ , was measured using a linear encoder with 600 PPR (pulses per revolution). The encoder was placed at $X_1 = 1.48$ m and $Z_1 = 1.53$ m from the bearing axis. The measuring wire was linked to the flap by a vertical aluminium frame (see Fig. 2). The variation of rotation angle of the flap with time, $\theta(t)$, can be calculated by the following implicit equation:

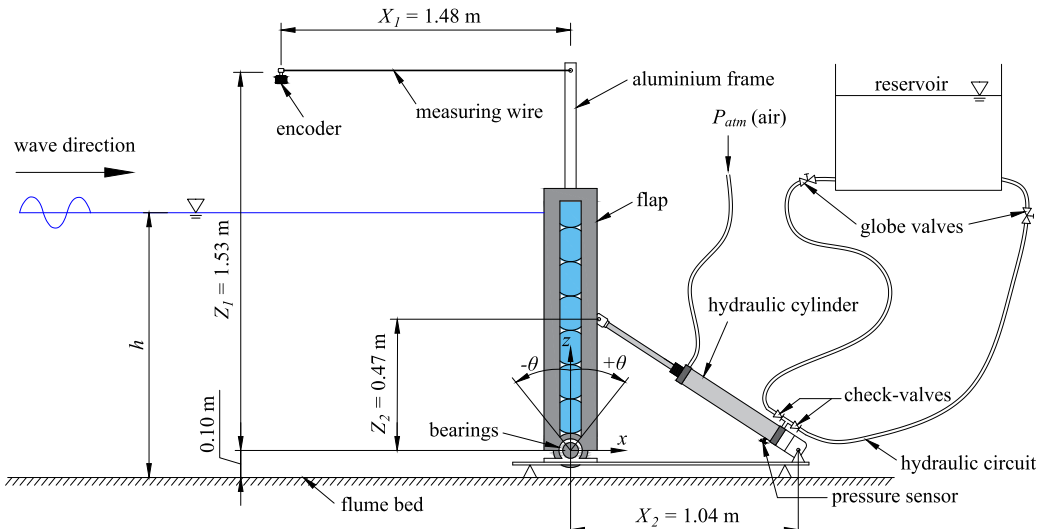
**Fig. 3.** Schematic sketch of the side view of OWSC model (not to scale).

Table 2

Wave conditions used for the regular wave tests.

<i>T</i> (s)	<i>L</i> (m)	<i>kh</i>	<i>kH</i>
2	4.9	1.058	0.192 0.224 0.256 0.289 0.321 0.353 0.385
2.25	5.7	0.910	0.165 0.193 0.221 0.248 0.276 0.303 0.331
2.5	6.48	0.799	0.145 0.170 0.194 0.218 0.242 0.267 0.291
2.75	7.25	0.715	0.130 0.152 0.173 0.195 0.217 0.238 0.260
3	8.01	0.648	0.118 0.137 0.157 0.177 0.196 0.216 0.236
3.25	8.76	0.591	0.108 0.126 0.143 0.161 0.179 0.197 0.215
3.5	9.51	0.545	0.099 0.116 0.132 0.149 0.165 0.182 0.198
3.75	10.25	0.506	0.092 0.107 0.127 0.138 0.153 0.167 0.184
4	10.98	0.472	0.086 0.100 0.114 0.129 0.143 0.157 0.172

Table 3

Wave conditions used for the irregular wave tests.

Test	<i>T_p</i> (s)	<i>H_s</i> (m)	<i>H_m</i> (m)	<i>T_e</i> (s)	<i>T_m</i> (s)	<i>T_Z</i> (s)	<i>T_c</i> (s)	<i>P_w</i> (W m ⁻¹)
I1	3.6	0.25	0.15	3.4	2.5	1.7	0.2	88
I2	2.5	0.2	0.12	2.4	1.9	1.7	0.6	43
I3	3.6	0.15	0.09	3.3	2.6	2.1	0.3	30
I4	3.6	0.13	0.07	2.8	1.8	0.9	0.1	18

the integration of angular velocity given by the gyroscope and video tracker method. The relative error between these three methods was less than 1%. The angular velocity of the flap, $\dot{\theta}$, was calculated by an approximate differentiation of the measured θ . The noise in the calculated $\dot{\theta}$ signal was filtered by a causal low-pass filter with a bandwidth of 2 Hz cut-off frequency [31]. The water pressure inside the cylinder chamber, P_c , was measured using a pressure sensor with an accuracy less than 0.2% RO (rated output). The pressure sensor and encoder were connected to a data-acquisition system with an 8-bit A/D converter.

The free-surface elevation, η , was measured in the central line of the wave flume ($y = 0$) by four standard capacitive wave probes (WP1, WP2, WP3 and WP4 in Fig. 1a). WP1, WP2 and WP3 were placed upstream of the flap for the separation of incident and reflected waves, by using the three-point method proposed by Ref. [32]. WP4 was placed downstream of the flap to measure the transmitted waves. The distance between WP1 and WP2, x_{12} , and between WP2 and WP3, x_{23} , were chosen according to the method of [32]. The value of x_{12} and x_{23} used for regular wave and for irregular wave tests are shown in Tables 4 and 5, respectively. In this study, five equally-spaced water submersion of each wave probe were used for its static calibration. A first-order calibration polynomial relating the output voltages to the η was obtained by a least-square fit procedure [33].

In order to assess the reflection coefficient of the beach, tests were also performed without the OWSC in the wave flume. The reflection analysis was carried out using a Matlab routine. Due to the high absorption efficiency of the beach, reflection coefficients were less than 8%. This level of wave reflection is difficult to avoid in wave flume testing [18,34].

The wave probes were connected to a data-acquisition system with an 8-bit A/D converter. The sampling frequency for η was 25 Hz, while for the other signals was 100 Hz. The duration of each test is approximately 300 s for regular waves and 3000 s for irregular waves. The synchronisation between the wavemaker and data acquisition systems for free-surface elevation and other signals was performed using an external trigger. The synchronisation was checked by comparing the signals from the wave probes and the encoder.

The instantaneous power capture of the OWSC, W_{out} , is evaluated by $W_{out}(t) = P_c(t)Q(t)$, where Q is the flow rate in the hydraulic circuit, calculated based on the relative velocity between piston and cylinder, \dot{x} , as:

$$Q(t) = A\dot{x}(t) \quad (2)$$

where A is the cross-section area of the cylinder chamber (with bore diameter of 0.063 m). The relative velocity between piston and cylinder can be calculated based on the $\dot{\theta}$ as:

$$\dot{x}(t) = \cos \left[\theta(t) + \tan^{-1} \frac{1}{X_2 \cos \theta(t)} \right] Z_2 \dot{\theta}(t) \quad (3)$$

where $X_2 = 1.04$ m is the horizontal distance between flap and

$$[X_1 - \Delta X_1(t)]^2 = X_1^2 + \left[2Z_1 \sin \frac{\theta(t)}{2} \right]^2 - 2X_1 Z_1 \sin \theta(t) \quad (1)$$

where t is the time and ΔX_1 is the variation of the length of the measuring wire. This method was also used by Ref. [31]; where the rotation angle of the flap obtained by encoder was validated against

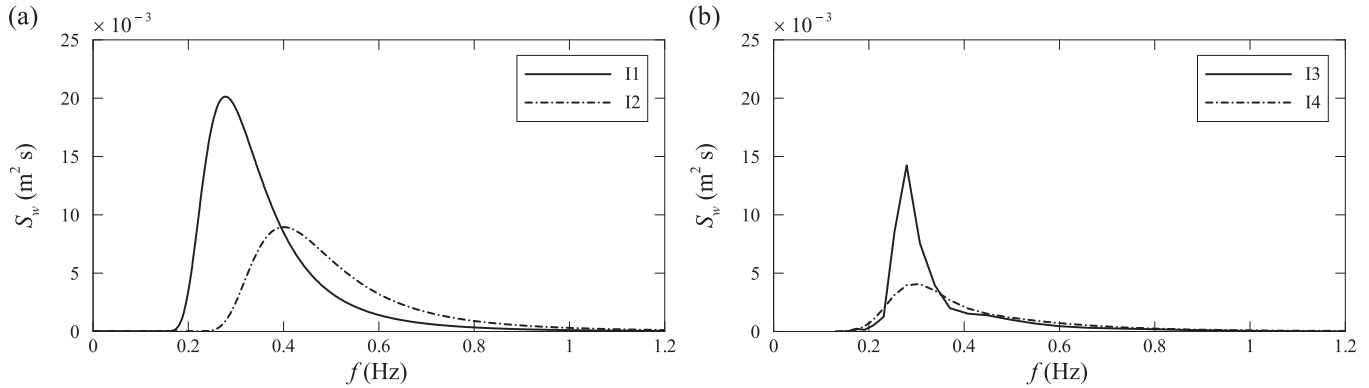


Fig. 4. Input signals to the wavemaker: (a) JONSWAP spectrum (tests I1 and I2); (b) field spectrum (tests I3 and I4).

Table 4

Distances between wave probes used for the regular wave tests.

\$T\$ (s)	\$x_{12}\$ (m)	\$x_{23}\$ (m)
2	0.49	1.23
2.25	0.57	1.42
2.5	0.65	1.62
2.75	0.72	1.81
3	0.8	2
3.25	0.88	2.19
3.5	0.95	2.38
3.75	1.02	2.56
4	1.1	2.75

Table 5

Distances between wave probes used for the irregular wave tests.

Test (s)	\$x_{12}\$ (m)	\$x_{23}\$ (m)
I1	0.62	1.62
I2	0.98	2.45
I3	0.98	2.45
I4	0.98	2.45

cylinder body bearings and \$Z_2 = 0.47\$ m is the vertical distance between flap and piston rod bearings (see Fig. 3).

The time-averaged power capture, \$\overline{W}_{out}\$, is determined as:

$$\overline{W}_{out} = \frac{1}{t_{total}} \int_0^{t_{total}} P_c(t) Q(t) dt \quad (4)$$

where \$t_{total}\$ is the duration of the test without the ramp-up period.

According to the linear wave theory, for regular waves the mean incident power per unit width is defined by:

$$\overline{W}_i = \frac{1}{8} \rho g H^2 c_g \quad (5)$$

where \$\rho = 1000\$ kg m\$^{-3}\$ is the water density, \$g = 9.81\$ m s\$^{-2}\$ is the gravitational acceleration and \$c_g\$ is the wave group velocity. For the intermediate water depth wave condition studied, \$c_g\$ is given by:

$$c_g = \frac{\omega}{2k} \left(1 + \frac{2kh}{\sinh 2kh} \right) \quad (6)$$

where \$\omega = 2\pi f\$ is the wave angular frequency, \$f\$ is the wave frequency and \$k\$ is given by the dispersion relationship as \$\omega^2 = gk \tanh(kh)\$.

For unidirectional irregular waves the mean incident power per

unit width, \$\overline{W}_i\$, is defined as:

$$\overline{W}_i = \rho g \int_0^\infty c_g(f) S_\eta(f) df \quad (7)$$

where \$S_\eta\$ is the power spectrum of the incident waves.

A common way to indicate the power capture capability of any wave energy converter (WEC) device is the CWR [35], defined as:

$$CWR = \frac{\overline{W}_{out}}{\overline{W}_i B} \quad (8)$$

The ratio of the mean reflected wave power, \$\overline{W}_r\$, and \$\overline{W}_i\$ is one of the possible alternatives to estimate the performance of the OWSC, defined as:

$$\varepsilon = \frac{\overline{W}_r}{\overline{W}_i} \quad (9)$$

3. Experimental results of OWSC under regular waves

In order to illustrate the experimental results of the OWSC under regular waves, the measured \$\eta\$ obtained from WP3 and WP4 together with \$\theta\$, \$P_c\$ and \$W_{out}\$ for \$T = 2.5\$ s and \$H = 0.20\$ m (corresponding to \$kh = 0.194\$ and \$kh = 0.799\$) and for \$T = 3\$ s and \$H = 0.25\$ m (corresponding to \$kh = 0.196\$ and \$kh = 0.648\$, see Table 2) are presented in Fig. 5.

From Fig. 5a and b, it is clear that the \$\eta\$ shows a nonlinear behavior, caused by the wave interactions with OWSC and flume. Such interactions cause differences between incident plus reflected waves (measured by WP3) and transmitted waves (measured by WP4) for both cases. It was observed that the wave amplitude decreases close to the flap by approximately 45% for \$T = 2.5\$ s and \$H = 0.20\$ m, and to 30% for \$T = 3\$ s and \$H = 0.25\$ m. This phenomenon is caused by the ascendant flows when the wave crest starts to approach the flap, which are caused by the combined effect of blockage [36] and wave overtopping [37].

In terms of wave cycle, as the wave crest approaches the OWSC, the flap starts to move toward the beach with \$\dot{\theta} > 0\$ (Fig. 6a). The flap reaches its maximum \$\dot{\theta}\$ when the wave crest begins to pass over it (Fig. 6b). Once the flap is fully submerged, \$\dot{\theta}\$ decreases rapidly and then the flap stops. As the wave crest moves away from the flap, the wave pressure is reduced and the water level begins to drop as the trough approaches and the flap begins to rise up and pierces through the back of the wave crest (Fig. 6c). As the wave comes to the trough, the flap is moving towards the wavemaker with \$\dot{\theta} < 0\$.

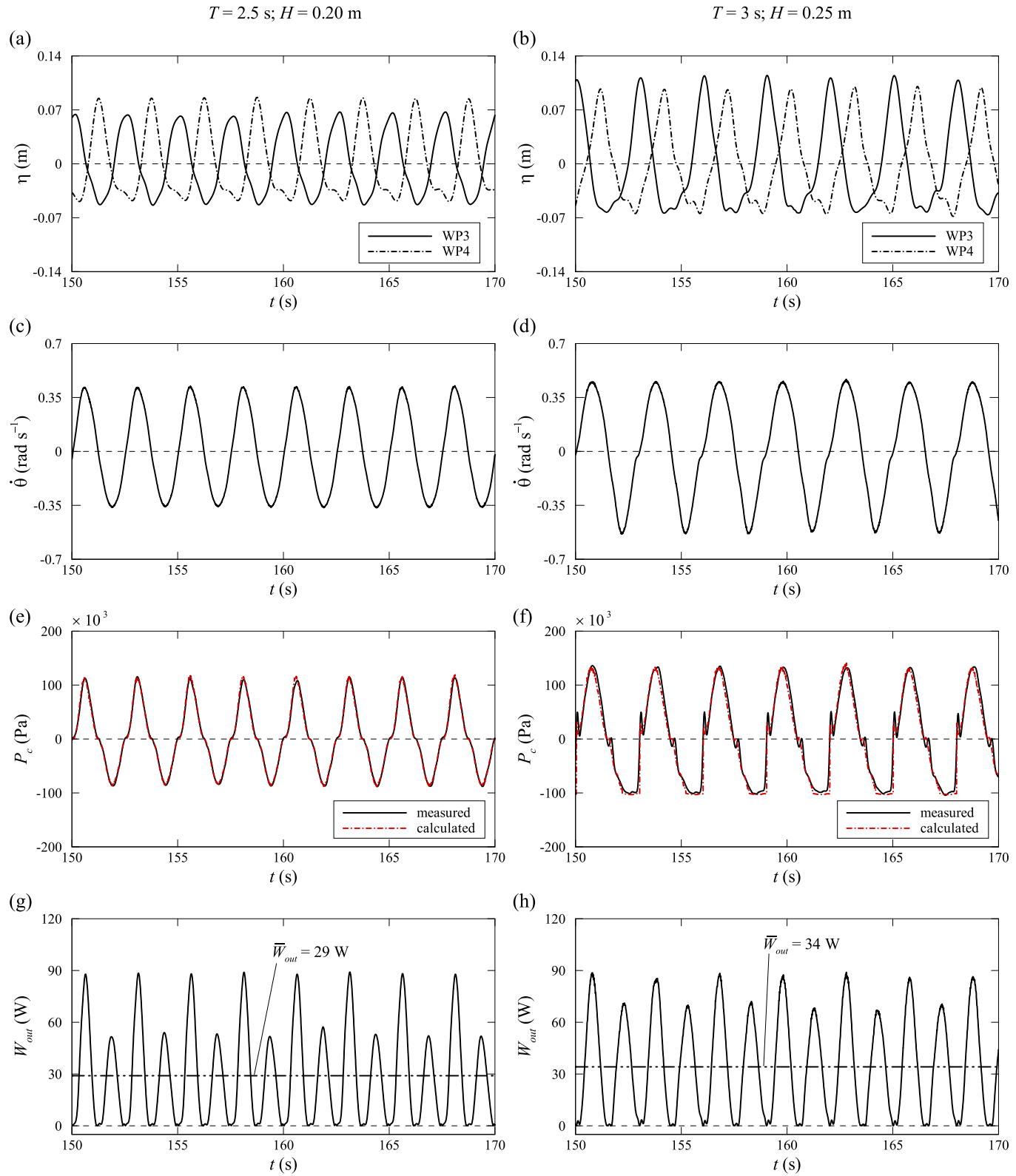


Fig. 5. Detail of the time series: (a,b) free-surface elevation measured by WP3 and WP4; (c,d) angular velocity of the flap; (e,f) pressure in the cylinder chamber; (g,h) power capture. The left column shows time series for $T = 2.5 \text{ s}$ and $H = 0.20 \text{ m}$, and the right column for $T = 3 \text{ s}$ and $H = 0.25 \text{ m}$. In (e,f) the measured pressure in the cylinder chamber is fitted by Eq. (10). In (g,h) the horizontal dash-dotted line indicates the mean power capture.

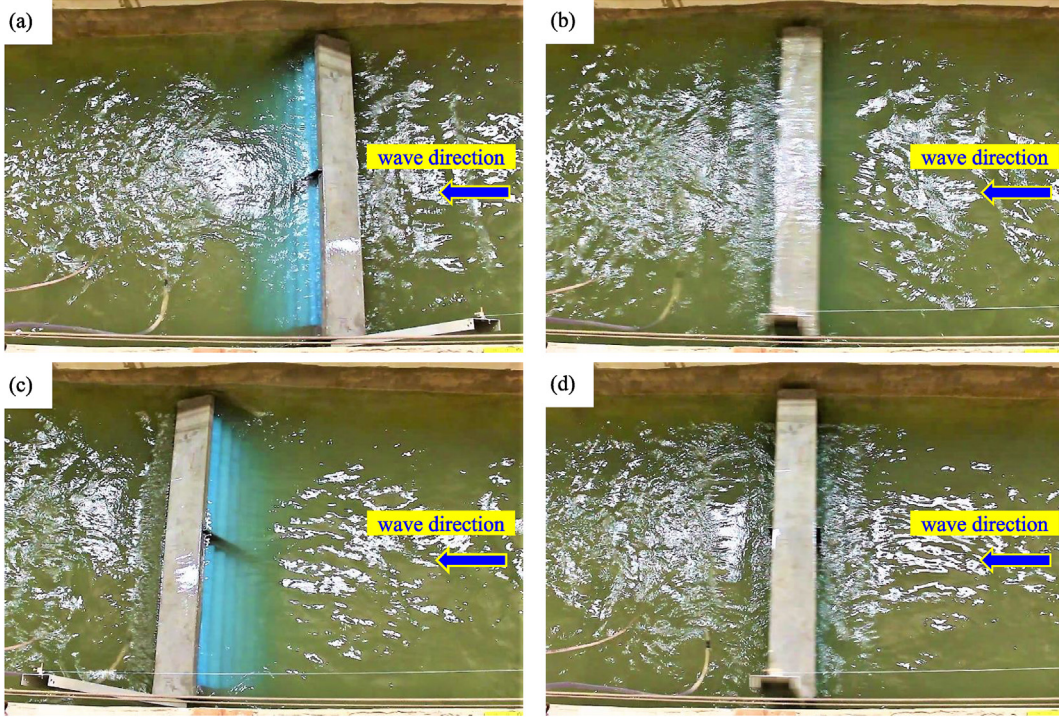


Fig. 6. Series of snapshots of the OWSC for $T = 3$ s and $H = 0.25$ m when: (a) wave crest approaches the OWSC; (b) wave crest begins to pass over the flap; (c) wave trough approaches the OWSC; (d) wave trough passes through the flap. The direction of wave propagation is from right to left.

The water level is low, much of the flap becomes exposed and, therefore, the water provides little resistance and the flap reaches its minimum $\dot{\theta}$ (Fig. 6d). Then the flap pitches forward into the incoming wave crest, and the wave cycle is repeated.

A more detailed view of wave-OWSC interaction can be seen in Fig. 6, where a series of snapshots of the OWSC for $T = 3$ s and $H = 0.25$ m is presented. Fig. 6a shows the instant when $\dot{\theta} \approx 0$ and the wave crest approaches the OWSC. The direction of wave propagation is from right to left. Fig. 6b shows the instant when the wave crest begins to pass over the flap. At this instant, the flap reaches its maximum $\dot{\theta} \approx 0.45$ rad s $^{-1}$. Fig. 6c shows the instant when $\dot{\theta} \approx 0$ and the wave trough approaches the OWSC. Fig. 6d shows the instant when the wave trough passes through the flap. At this instant, the flap reaches its minimum $\dot{\theta} \approx -0.54$ rad s $^{-1}$.

In order to investigate the nonlinear effects, the harmonic decompositions of η , $\dot{\theta}$ and P_c for the conditions presented in Fig. 5 are shown in Figs. 7 and 8. In this decomposition fourth-order harmonic components (i.e., linear, double, triple and quadruple frequency components) are necessary to describe the main wave-OWSC interactions [22]. In fact, the effect of local nonlinearities such as viscous damping is significant, any contribution from this drag term would produce linear and triple frequency components [38].

As expected, qualitatively, the structure of the measured time series are dominated by the linear component. However, the signals present some important double and triple frequency components. In general, the quadruple frequency component is slightly smaller than the other components. However, for the P_c with $T = 3$ s and $H = 0.25$ m this quadruple frequency component presents a higher value (Fig. 8c), caused by the cavitation phenomena observed in the expansion phase of the hydraulic cylinder ($\dot{\theta} < 0$). As cavitation plays important roles in the P_c variation, it is fitted by the following model:

$$P_c = \begin{cases} K_p \dot{\theta}^2 + I_p \ddot{\theta} & \text{for } \sigma \geq 0 \text{ (no cavitation)} \\ P_v & \\ + I_p \ddot{\theta} & \text{for } \sigma < 0 \text{ (cavitation)} \end{cases} \quad (10)$$

where K_p is the coefficient of pressure loss, I_p is the coefficient that takes into account the inertia of the fluid [31,39] and P_v is the vapor pressure of water. In this model, σ is defined as:

$$\sigma = \frac{P_{atm} + P_c - P_v}{P_{atm}} \quad (11)$$

In a perfect PTO system, K_p would be constant but this was not the case. K_p is dependent on the flow regime in the hydraulic circuit, and presents different values for compression ($\dot{\theta} > 0$) and for expansion ($\dot{\theta} < 0$) phases of the hydraulic cylinder (see Fig. 9). As referred in Sec. 2, the value of K_p was controlled by the valve-opening, and was quantified based on the number of rotations of the globe valves on the handwheel, M . In this paper, the experimental tests were performed for six valve-openings ($M = 0, 1, 2, 3, 4$ and 5) for $\dot{\theta} > 0$ and for a full valve-opening ($M = 0$) for $\dot{\theta} < 0$. $M = 5$ corresponds to the maximum pressure range of the hydraulic cylinder. An example of the variation of K_p with magnitude of $\dot{\theta}$ for $T = 3$ s and $H = 0.25$ m is shown in Fig. 9.

As expected for both phases of the hydraulic cylinder, K_p presents the typical transition region between laminar and turbulent flows. However, in the turbulent flow regime the K_p is almost constant (Fig. 9). The transition region is characterized by a complex variation of K_p , and due to the lack of information concerning its physical characteristics, the measured P_c in Fig. 5e and f are fitted using a constant value of K_p in the turbulent flow. The calculated P_c shows a good agreement with measured data with the least squares goodness-of-fit $R^2 \approx 0.98$ for $T = 2.5$ s and $H = 0.20$ m (Fig. 5e). In

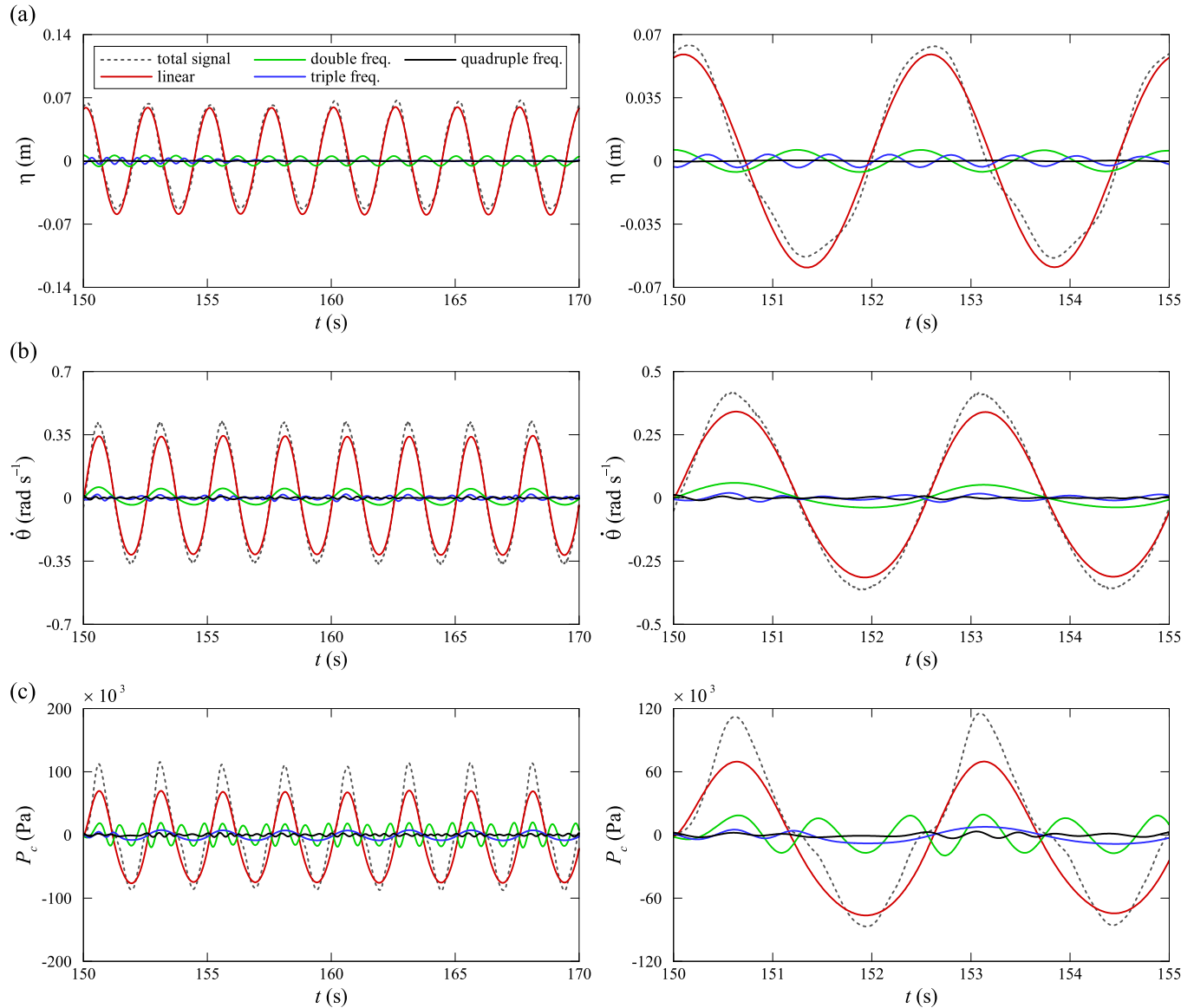


Fig. 7. Harmonic decomposition for $T = 2.5$ s and $H = 0.20$ m: (a) free-surface elevation measured by WP3; (b) angular velocity of the flap; (c) pressure in the cylinder chamber. The right column shows in detail two wave period.

Fig. 5f, for $T = 3$ s and $H = 0.25$ m, some discrepancy is observed for $\dot{\theta} \approx 0$, which may be because of the dissolution of cavitation bubbles. The association between cavitation bubbles and the strong nonlinear behavior of wave-OWSC interaction causes the steep gradient of P_c (**Fig. 5f**). However, the calculated P_c shows a good agreement with experimental data with $R^2 \approx 0.95$. Furthermore, this steep gradient of P_c is absorbed in the W_{out} (**Fig. 5h**), as its occurs for small values of $\dot{\theta}$. The experimental and calculated \bar{W}_{out} presents a relative error about 2%.

In order to investigate the nonlinear behavior of the wave-OWSC interaction the RAO is introduced. The RAO describes a linear relationship between the resultant motion response and the incident wave amplitude [38], in this study, RAO was obtained by evaluating the magnitude of $\dot{\theta}$ and η . Similarly to Ref. [29]; due to the asymmetry of the flap motion (i.e., $|\dot{\theta}_{max}| \neq |\dot{\theta}_{min}|$), the RAO is defined as:

$$\text{RAO} = \frac{|\dot{\theta}_{max} - \dot{\theta}_{min}|}{H} \quad (12)$$

where $\dot{\theta}_{max}$ and $\dot{\theta}_{min}$ are the maximum and minimum of $\dot{\theta}$, respectively. The variation of the RAO with wave frequency, f , and with coefficient of pressure loss, K_p , for different wave conditions are presented in **Fig. 10**. The variation of the RAO with f in **Fig. 10a** is obtained for $K_p = 6.5 \times 10^5 \text{ Pa s}^2$ (i.e., for one rotation of the globe valves on the handwheel, $M = 1$) in the compression phase and for $K_p = 3.3 \times 10^5 \text{ Pa s}^2$ (i.e., for a full valve-opening, $M = 0$) in the expansion phase of the hydraulic cylinder, and for three different $H = 0.2, 0.25$ and 0.3 m. It can be seen that the RAO decreases with increasing H , which may be due to the wave overtopping and viscous effects that increases with the increasing of H . These viscous effects act as a loss mechanism and for large Keulegan-

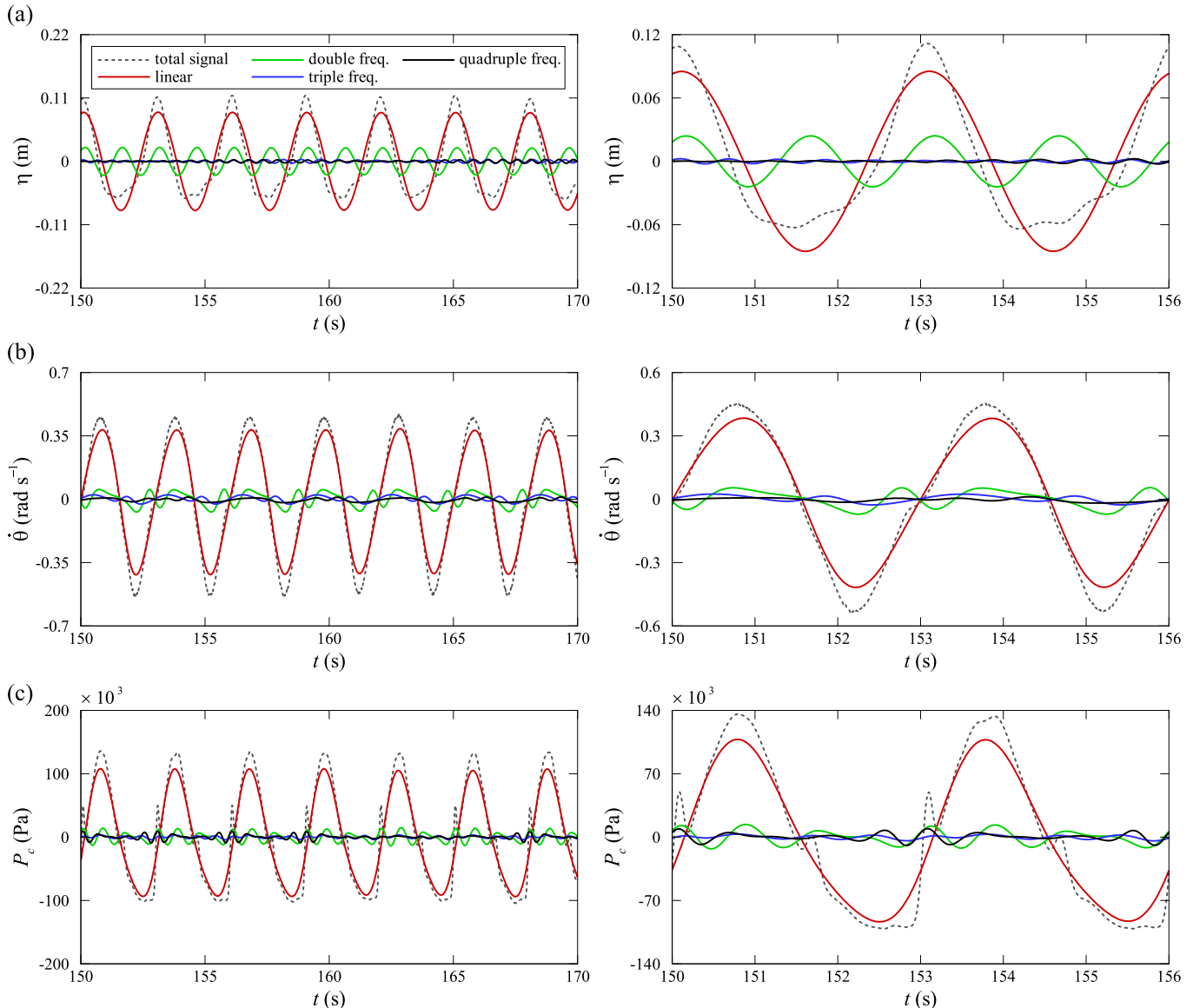


Fig. 8. Harmonic decomposition for $T = 3$ s and $H = 0.25$ m: (a) free-surface elevation measured by WP3; (b) angular velocity of the flap; (c) pressure in the cylinder chamber. The right column shows in detail two wave period.

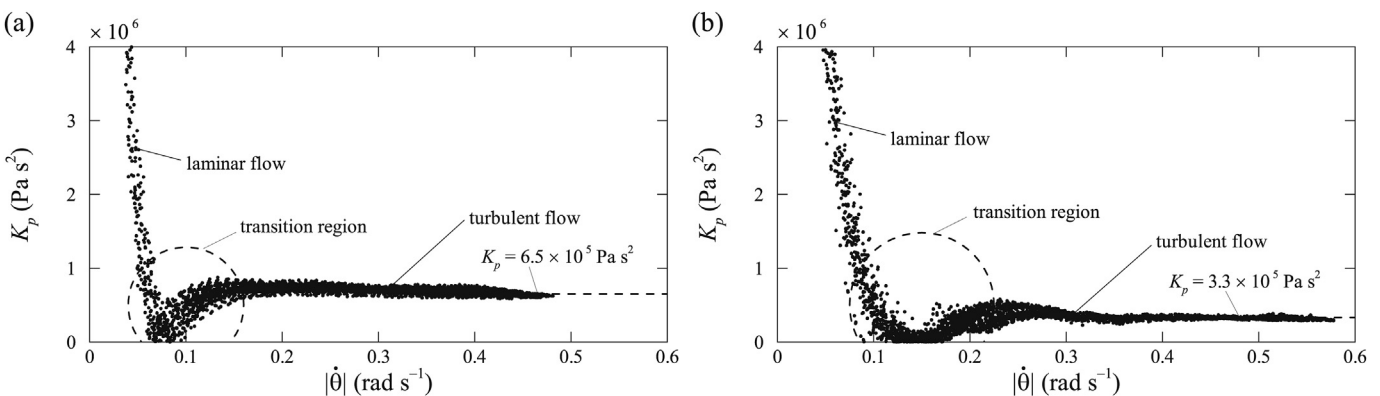


Fig. 9. Variation of the coefficient of pressure loss with magnitude of angular velocity of the flap for $T = 3$ s and $H = 0.25$ m in: (a) compression phase of the hydraulic cylinder ($\dot{\theta} > 0$) for $M = 1$; (b) expansion phase of the hydraulic cylinder ($\dot{\theta} < 0$) for $M = 0$.

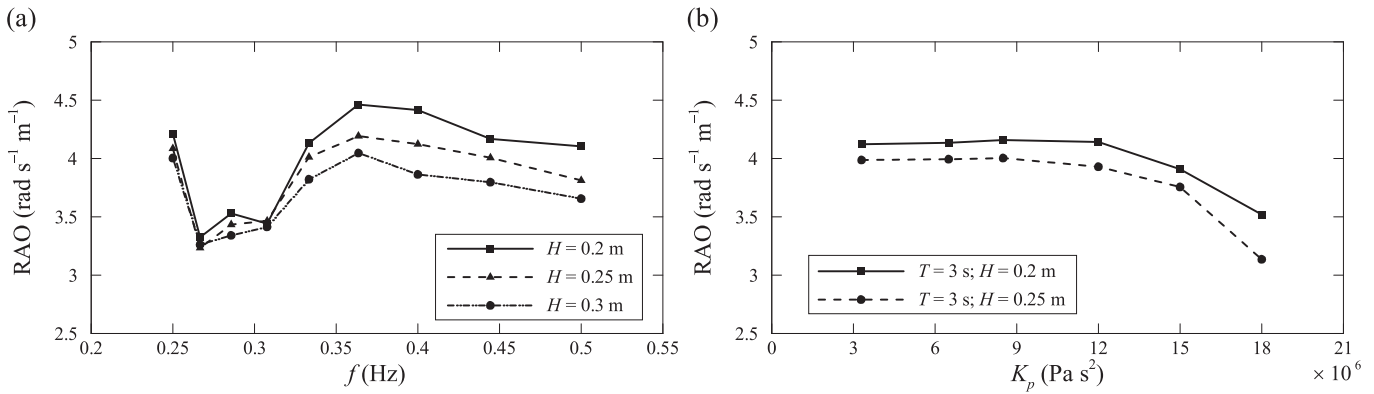


Fig. 10. Variation of the RAO with: (a) wave frequency; (b) coefficient of pressure loss.

Carpenter number they become relatively more relevant than the wave surge force acting on the flap, resulting in the reduced RAO [40]. [19] have shown that increasing the *f* can increase the wave surge force, as shorter waves (i.e., higher *f*) experience larger horizontal water particle acceleration. However, in Fig. 10a the RAO does not significantly increase with increases of *f*. This is caused by the latching effect of the PTO system, which limits the flap dynamic.

In Fig. 10b the variation of the RAO with *K_p* are obtained for *T* = 3 s and *H* = 0.2 and 0.25 m, corresponding respectively to *kH* = 0.157 and 0.196, and *kh* = 0.648 (see Table 2). The *K_p* does not appreciably change the RAO for *K_p* < 12 × 10⁵ Pa s², however when the *K_p* increases further a large variation of the RAO is observed (from *K_p* = 12 × 10⁵ to 18 × 10⁵ Pa s² the RAO is reduced to approximately 20%), due to the increases of a latching effect of the hydraulic PTO system where the flap remains stationary for as long as the hydrodynamic forces on its wetted surface are unable to overcome the resisting force introduced by the PTO system.

Fig. 11 shows the variation of CWR and ε with *f* and with *K_p* in the same conditions presented in Fig. 10. It can be seen that ε decreases with increasing of *H*, showing almost the same trend of RAO except for the low values of *f* (see Figs. 10a and 11a). However the CWR does not seem to vary excessively with *H*, showing variation range less than 15%. The comparison of ε and CWR shows that ε is much larger than the CWR, about 30% (Fig. 11a). An explanation for this behavior is the increase of reflection due to the forcing moment onto the flap. This behavior can be confirmed in Fig. 11b where ε increases as *K_p* increases. The measurement of ε is not accurate to predict the trends of the CWR.

In order to better understand the influence of the *H* and *f* on the

results, the variation of CWR, RAO and amplitude of hydraulic torque, *T_H*, with respect to *H* and *f* are plotted in Fig. 12. The *T_H* is calculated from the *P_c*. In general, it can be confirmed that the influence of the *H* is less significant on CWR than on *f*. However, both *f* and *H* have a large effect on RAO, with higher values being obtained for 0.35 ≤ *f* ≤ 0.45 Hz and for 0.15 ≤ *H* ≤ 0.2 m. The results clearly show that for any given *f*, the *T_H* increases as the *H* increases. It can be concluded that there is a weak correlation between CWR, RAO and *T_H*.

4. Experimental results of OWSC under irregular waves

In order to illustrate the experimental results, an example of the time series of η , $\dot{\theta}$ and *P_c* and the respective spectrum *S_η*, *S_{θ̇}* and *S_P* for test I1 (see Table 3) are shown in Fig. 13. It is clear that the η and $\dot{\theta}$ show a strong nonlinear behavior, caused by the wave interactions with OWSC and flume. Such interactions cause differences between incident and reflected waves measured by WP1 and therefore a nonlinear dependence between η and $\dot{\theta}$ (Fig. 13a and b). The measured *P_c* is fitted by the model presented in Eq. (10). The calculated *P_c* shows a good agreement with measured data, with typical value of $R^2 \approx 0.92$ (Fig. 13c). As for regular waves the model captures most of the dynamic behaviors of *P_c*, including the cavitation in the hydraulic PTO system. The time series of *W_{out}* is presented in Fig. 14. For this test condition $\bar{W}_{out} = 20$ W and CWR = 17% are obtained.

In order to analyse the dynamic behavior of the OWSC under irregular waves the RAO is also used. However, as RAO describes the linear relationship between the resultant response and the incident

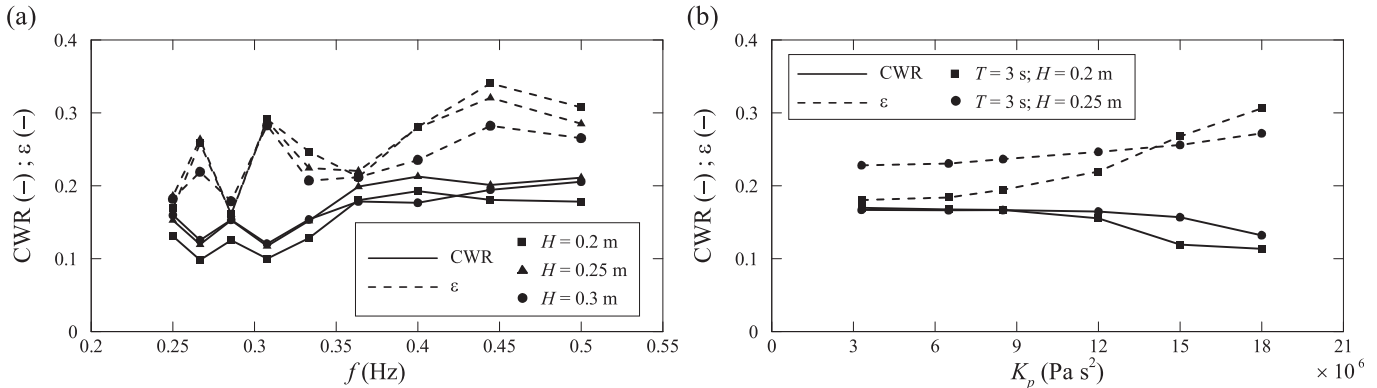


Fig. 11. Variation of CWR and ratio of the mean reflected wave power with: (a) wave frequency; (b) coefficient of pressure loss.

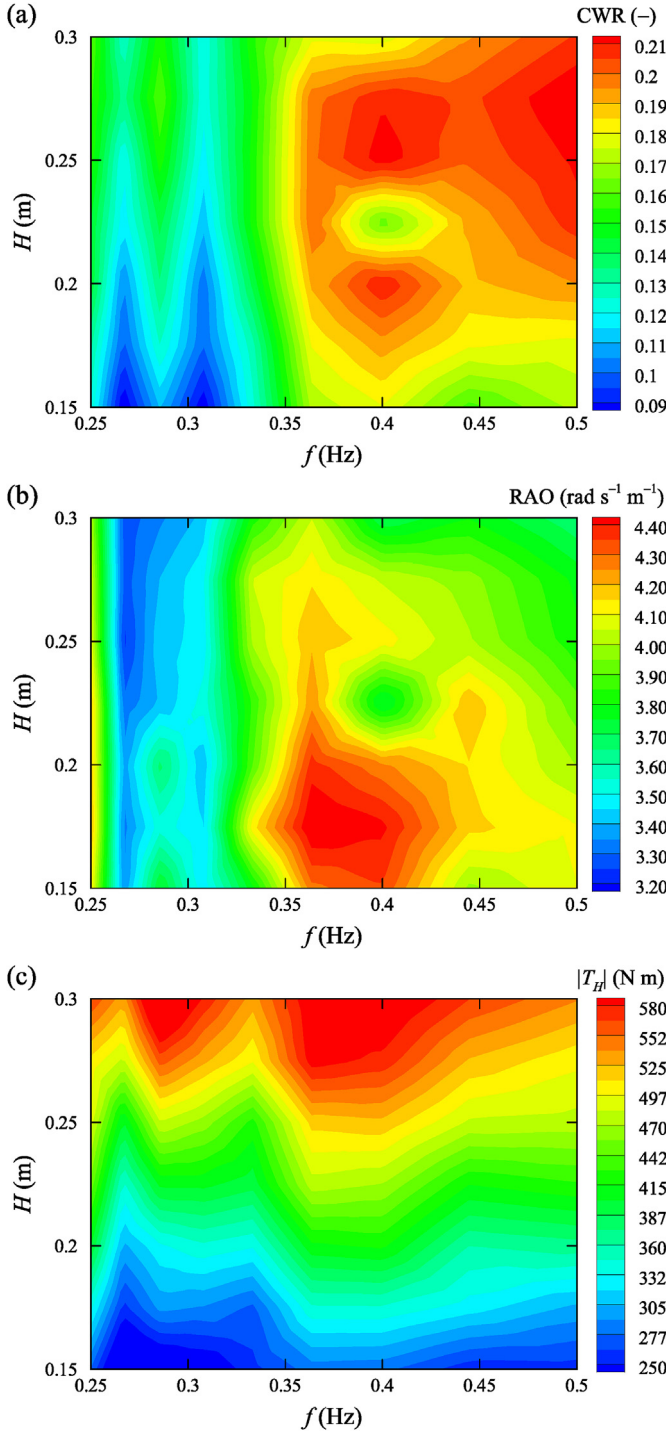


Fig. 12. Contour plot of CWR, RAO and hydraulic torque as a function of wave height and frequency: (a) CWR; (b) RAO; (c) hydraulic torque.

wave amplitude [38], in this study, RAO was obtained by evaluating the magnitude of the linear component of $\dot{\theta}$ and η , as:

$$\text{RAO}(f) = \sqrt{\frac{S_{\dot{\theta}}(f)}{S_{\eta}(f)}} \quad (13)$$

where $S_{\dot{\theta}}$ and S_{η} are the power spectrum of the first-harmonic $\dot{\theta}$ and

η , respectively. The incident η is obtained by the separation of incident and reflected waves, using the three-point method proposed by Ref. [32]. Fig. 15 shows the harmonic decompositions of measured η , $\dot{\theta}$ and P_c in the same conditions presented in Fig. 13. Qualitatively, the structure of the signals are dominated by the linear component. However, as for regular waves, the signals contain important double and triple frequency components, especially for higher f . In fact, these higher-order components are more significant on the η for smaller f than $\dot{\theta}$ and P_c . An explanation for this behavior is the reflected waves and the 3D effects of the flume, that are more noticeable for a large measure time (3000 s).

As the higher-order frequency seems important, the nonlinear output frequency response functions, G_n , where $n = 2, 3$ and 4 is the order of harmonic decomposition, are considered as the extension of the RAO to the nonlinear case [41]. Fig. 16 shows the comparison of RAO and G_n for each test condition presented in Table 3.

The RAO curve is, for all test conditions, very similar in shape, except for low values of f where its variation seems to be a function of incident waves. In contrast to the linear wave theory, the RAO curve does not show a well-defined peak, showing a limited variation in a broadband with two small relative peaks at $f \approx 0.42$ and 0.84 Hz. The G_n also show a limited variation, presenting values of the same order of magnitude than RAO. Each average G_n show similar shapes for all test condition, however scattered than the RAO. This is presumably due to the effect of non-homogeneous interactions between G_n and possibly viscous damping for very large relative motion, which generally reduces the overall flap motion.

In order to investigate the effects of PTO system, the average RAO and G_n presented in Fig. 16 are compared with data obtained for $K_p = 12 \times 10^5 \text{ Pa s}^2$ and without PTO system in Fig. 17. As for regular waves, the RAO shows a small dependence with variation of K_p from 6.5×10^5 to $12 \times 10^5 \text{ Pa s}^2$. G_2 shows some differences just for $f < 1$ Hz. G_3 shows however a significant difference, with a shape slightly more asymmetric, hence more dependent on the K_p . G_4 seems to be almost independent on the K_p , with similar values for both K_p tested. Therefore, the effect of K_p produces double and triple frequency components. As expected, the PTO system introduces a large variation on the RAO, as the use of hydraulic PTO system provides a natural latching: the flap remains stationary for as long as the hydrodynamic forces on its wetted surface are unable to overcome the resisting force introduced by the PTO system. G_2 also shows a significant difference, hence more dependent on the effect of PTO system. G_3 and G_4 are weakly dependent on PTO damping.

5. Analysis of OWSC under irregular waves

In this section the effects of H_s and peak frequency, f_p , on the CWR are investigated. For a narrow-banded process, it should be possible to approximate the double, triple and quadruple frequency contributions in terms of the linear component as [38,42]:

$$\eta = A_{11}\eta_{11} + A_{22}\eta_{22} + A_{31}\eta_{31} + A_{33}\eta_{33} + A_{42}\eta_{42} + A_{44}\eta_{44} \quad (14)$$

and

$$\dot{\theta} = B_{11}\dot{\theta}_{11} + B_{22}\dot{\theta}_{22} + B_{31}\dot{\theta}_{31} + B_{33}\dot{\theta}_{33} + B_{42}\dot{\theta}_{42} + B_{44}\dot{\theta}_{44} \quad (15)$$

where A_{ij} and B_{ij} ($i, j = 1, 2, 3$ and 4) are the modified Stokes coefficients, η_{ij} and $\dot{\theta}_{ij}$ are the variables that contain both the

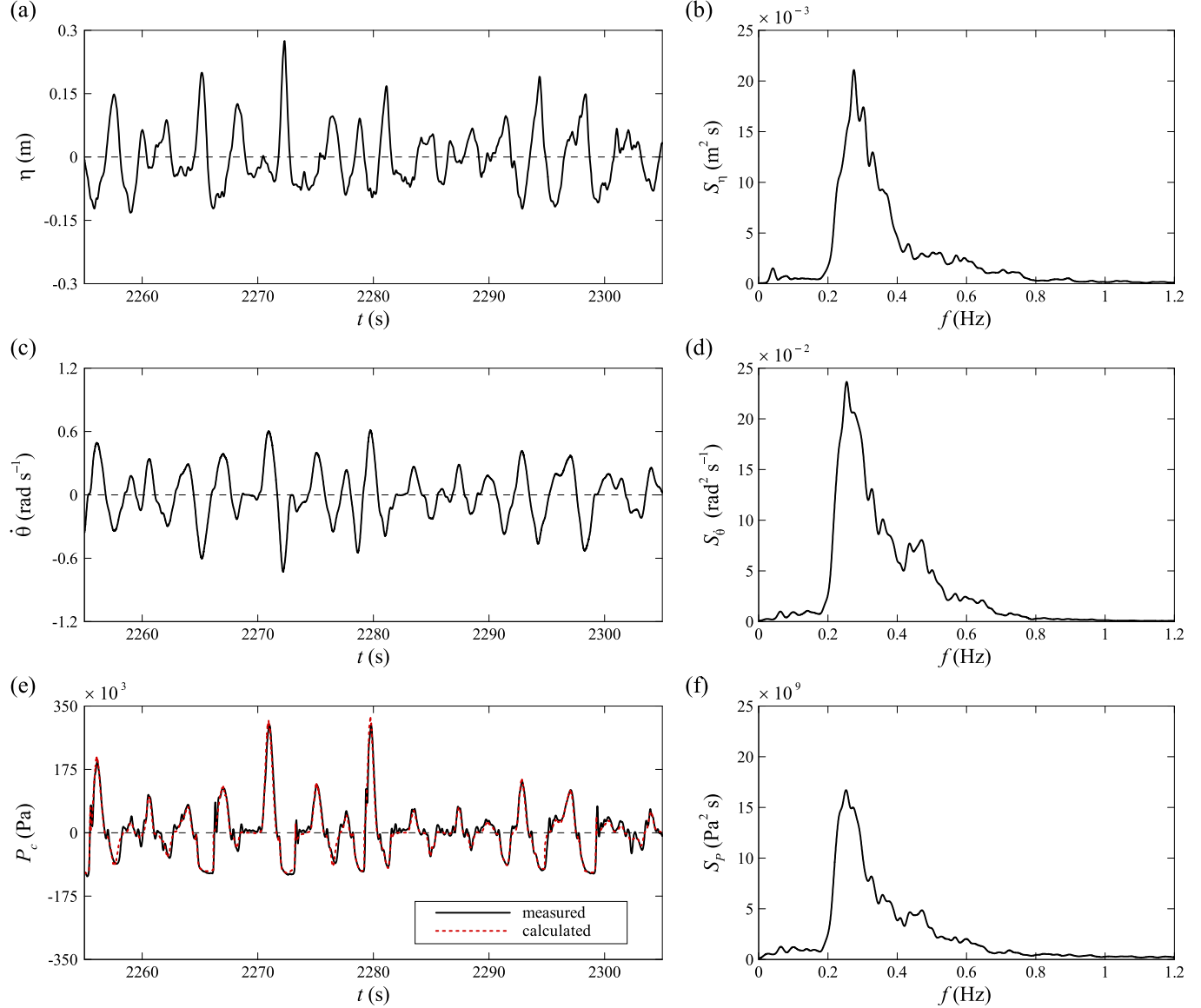


Fig. 13. Detail of the measured data for test I1. Time series: (a) free-surface elevation measured by WP1; (c) angular velocity of the flap; (e) pressure in the cylinder chamber. Power spectra: (b) free-surface elevation measured by WP1; (d) angular velocity of the flap; (f) pressure in the cylinder chamber.

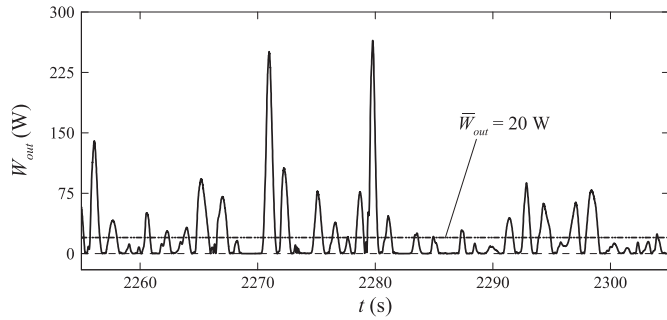


Fig. 14. Detail of the power capture for test I1. The horizontal dash-dotted line indicates the mean power capture.

amplitude and phase information and are defined in terms of the linear signal record, η_L and $\dot{\theta}_L$, and its Hilbert transform, η_{LH} and $\dot{\theta}_{LH}$, respectively. As an example, for η_{ij} is given by $\eta_{11} = \eta_L$; $\eta_{22} = \eta_L^2 - \eta_{LH}^2$; $\eta_{31} = \eta_L(\eta_L^2 + \eta_{LH}^2)$; $\eta_{33} = \eta_L(\eta_L^2 - 3\eta_{LH}^2)$; $\eta_{42} = (\eta_L^2 + \eta_{LH}^2)(\eta_L^2 - \eta_{LH}^2)$; $\eta_{44} = (\eta_L^2 - \eta_{LH}^2) - (2\eta_L\eta_{LH})^2$ [42]; and for $\dot{\theta}_{ij}$ it can be given analogously. In order to investigate the validity of this approximation, the double, triple and quadruple frequency components of η and $\dot{\theta}$ for test I1 are compared in Fig. 18.

Fig. 18 shows that the approximation of double, triple and quadruple frequency contributions in terms of the linear component cannot be used to provide a complete description of the output frequency response of wave-OWSC interaction with hydraulic PTO system. A large discrepancy is observed between measured and calculated solution of Eqs. (14) and (15), showing

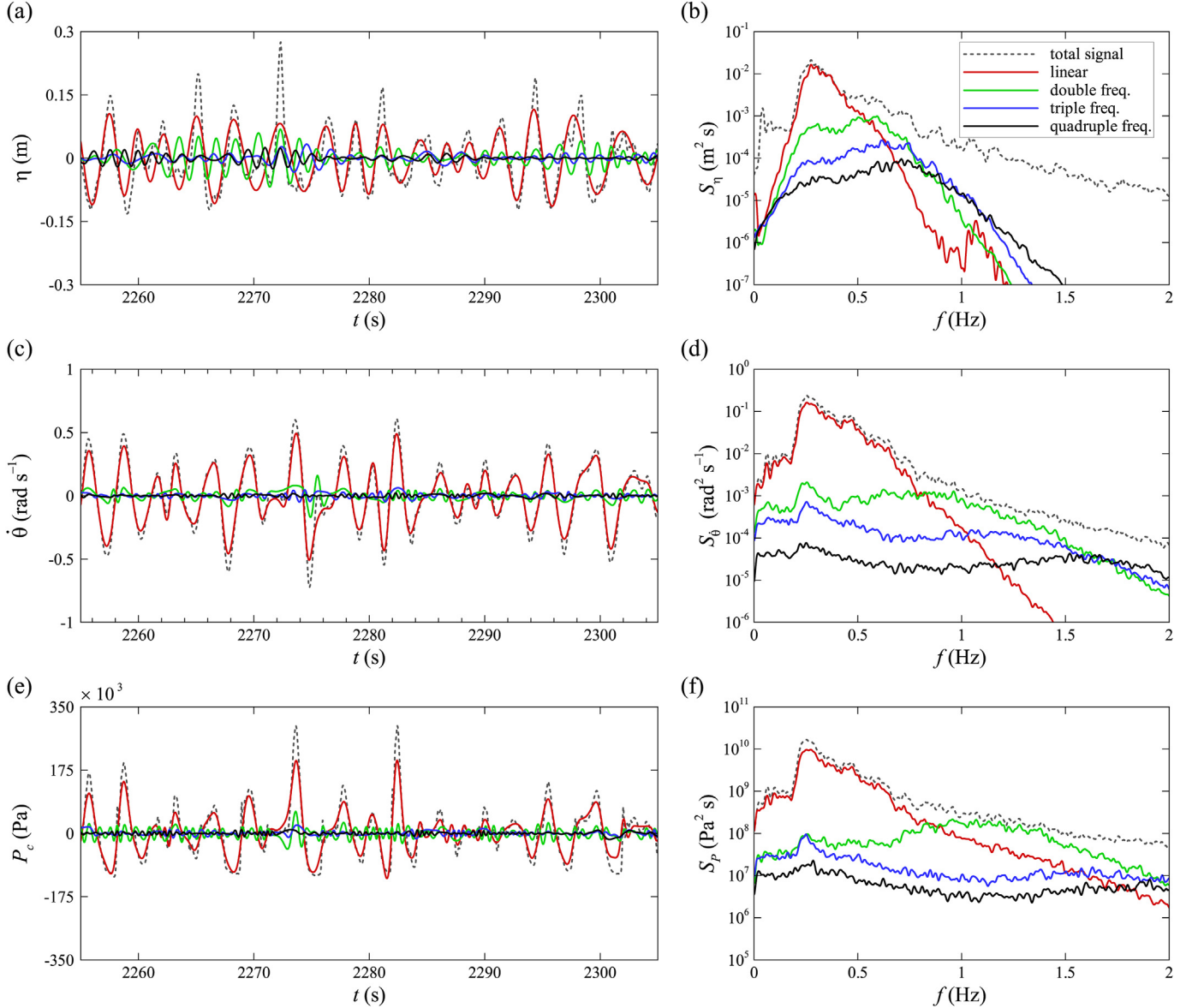


Fig. 15. Harmonic decomposition for test II. Time series: (a) free-surface elevation measured by WP1; (c) angular velocity of the flap; (e) pressure in the cylinder chamber. Power spectra: (b) free-surface elevation measured by WP1; (d) angular velocity of the flap; (f) pressure in the cylinder chamber.

that the OWSC higher-order frequency components of η and $\dot{\theta}$ are the effect of a combination of the output frequency responses of the involved homogeneous nonlinear systems [41]. Therefore, in this study, the higher-order generalized frequency response function are considered as the extension of the RAO to the nonlinear case. However, the relationship between the η and $\dot{\theta}$ spectra of nonlinear systems is much more complicated than in the linear system case. A new concept can be regarded as another extension of the linear frequency response function concept to the nonlinear case, which is a complement to the RAO, where $\dot{\theta}$ can be given by:

$$\dot{\theta}(f) = \text{RAO}(f)\eta_L(f) + \sum_{n=2}^4 G_n(f)\eta_n(f) \quad (16)$$

To predict the CWR of the OWSC under irregular waves this concept is used. The simulation of incident waves was performed using MATLAB. Firstly, for each H_s and f_p , S_η is determined by:

$$S_\eta(f) = \alpha H_s^2 \frac{f_p^4}{f^5} \exp\left[-\frac{5}{4} \frac{f_p^4}{f^4}\right] \gamma^{\beta(f)} \quad (17)$$

with

$$\alpha = \frac{0.0624}{0.23 + 0.0336\gamma - 0.185(1.9 + \gamma)^{-1}} \quad (18)$$

and

$$\beta(f) = \exp\left[-\frac{(f-f_p)^2}{2\sigma_i^2 f_p^2}\right] \quad (19)$$

where $\sigma_i = 0.07$ for $f \leq f_p$ and $\sigma_i = 0.09$ for $f > f_p$. Then the following decomposition is applied to simulate the η time series from a S_η :

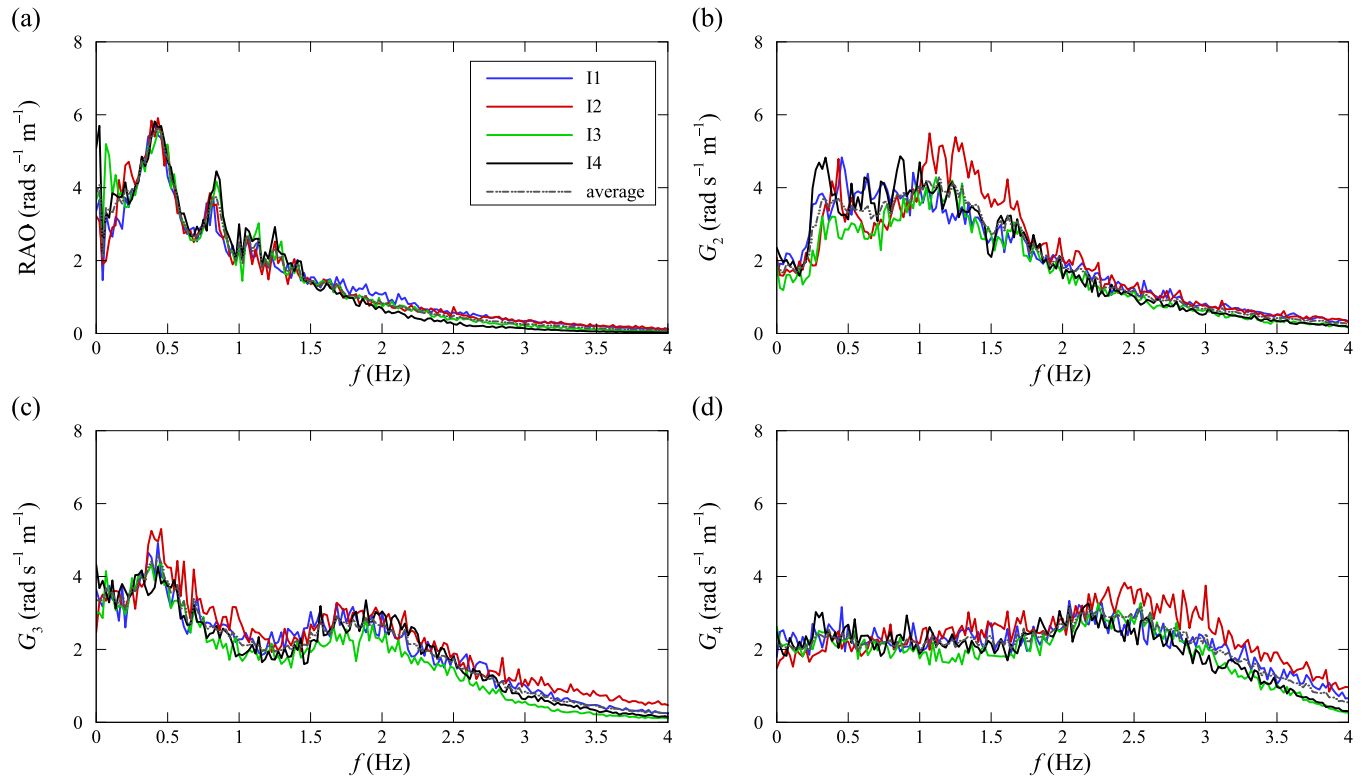


Fig. 16. Comparison of RAO and nonlinear output frequency response functions for each test condition presented in Table 3: (a) RAO; (b) second-order; (c) third-order; (d) fourth-order.

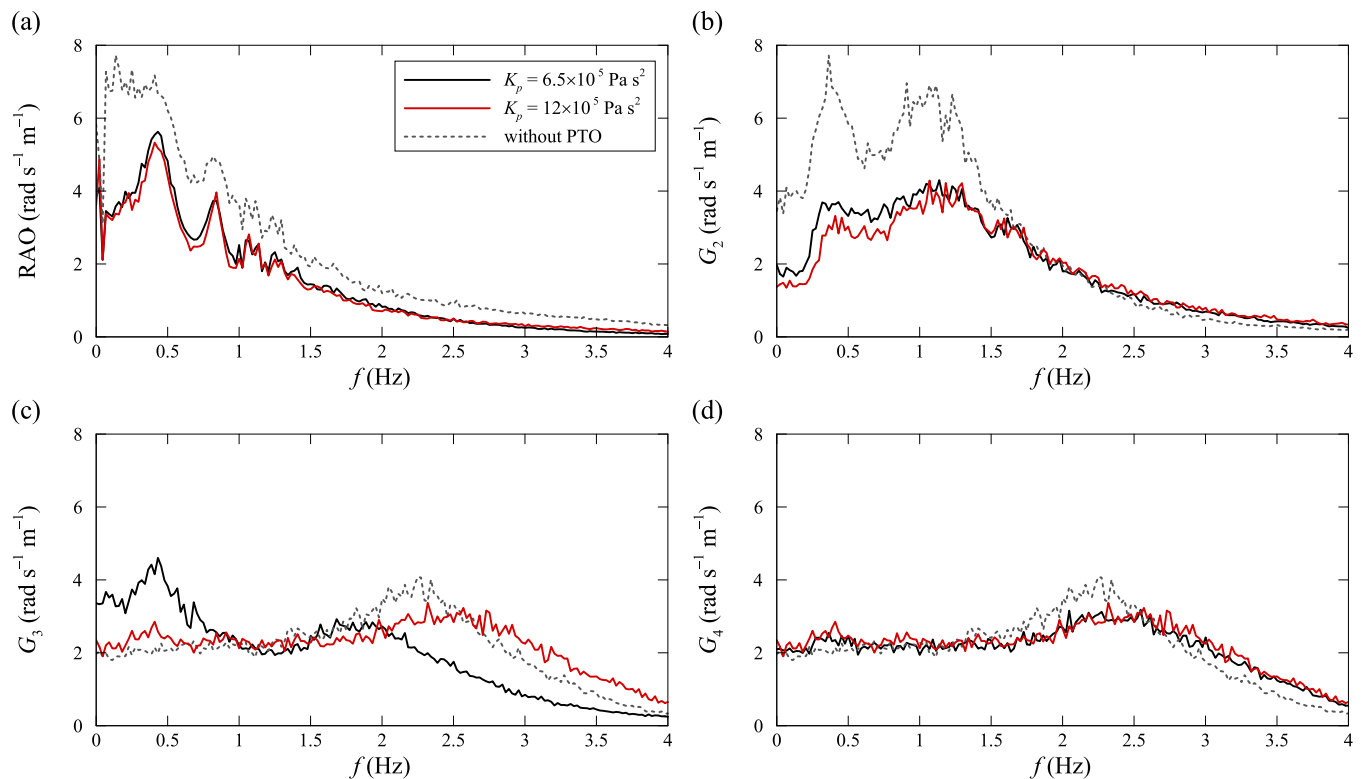


Fig. 17. Comparison of RAO and nonlinear output frequency response functions for $K_p = 6.5 \times 10^5$ and 12×10^5 Pa s 2 , and without PTO system: (a) RAO; (b) second-order; (c) third-order; (d) fourth-order.

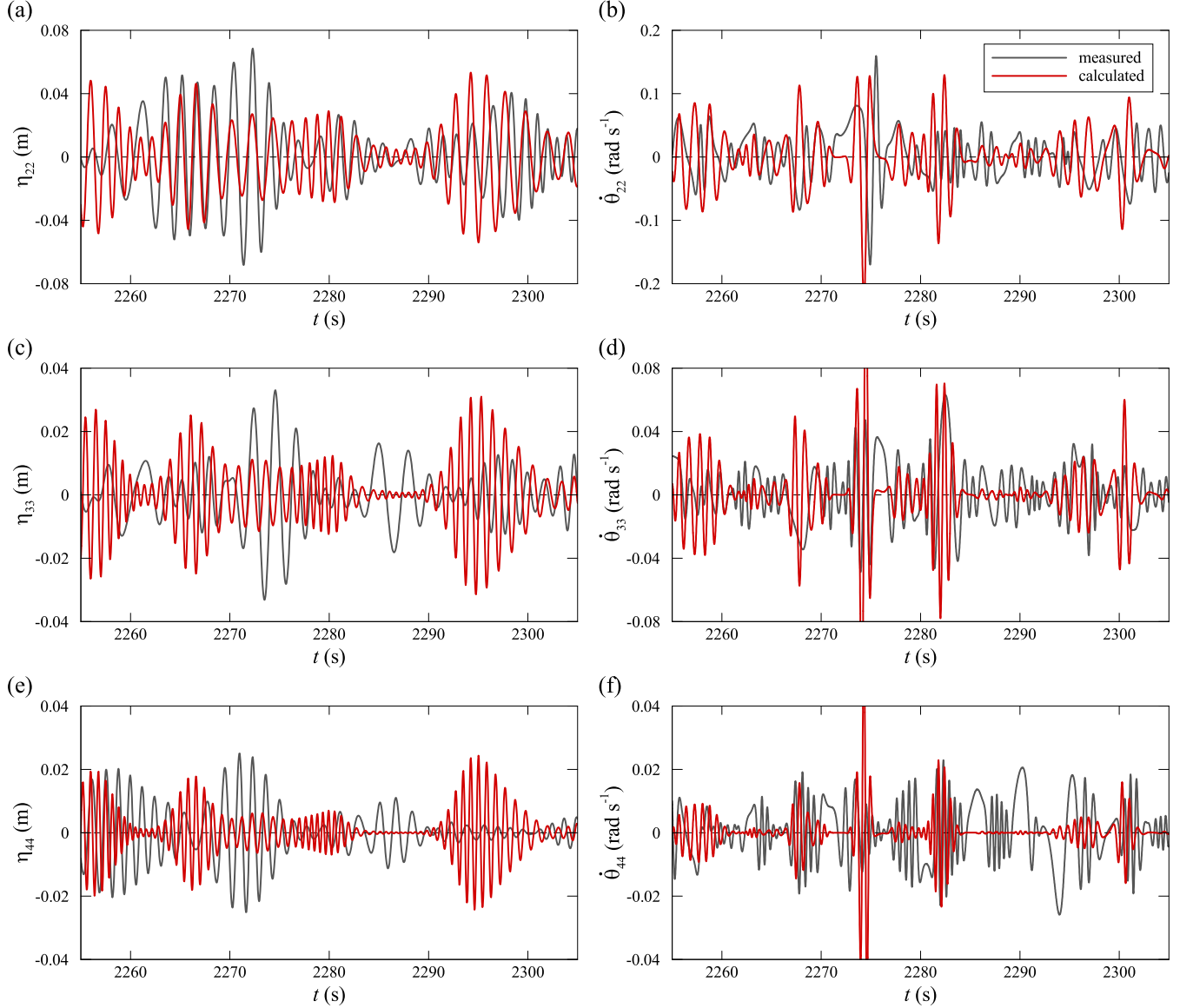


Fig. 18. Comparison of the higher frequency components of the free-surface elevation and angular velocity of the flap for test I1: (a,b) double; (c,d) triple; (e,f) quadruple frequency component.

$$\eta(t) = \sum_{n=1}^N A_n \cos(\omega_n t + \varepsilon_n) \quad (20)$$

where $\varepsilon \in [0; 2\pi]$ is the random wave phase and A_n is the wave amplitude of frequency n , given by:

$$A_n = \sqrt{2S_\eta(f_n)\Delta f} \quad (21)$$

Posteriorly, the harmonic decompositions of measured η are performed and $\dot{\theta}$ is calculated according to Eq. (16). Finally, P_c is calculated according to Eq. (10), CWR by Eq. (8) and \bar{W}_{out} by Eq. (4). In order to illustrate the computed results, two examples of the time series and power spectra of η and $\dot{\theta}$ for $\gamma = 1.2$ and 3.3 are shown in Fig. 19. These results are obtained for $H_s = 0.3$ m, $f_p = 0.42$ Hz and for $K_p = 6.5 \times 10^5$ Pa s² (i.e., for one rotation of the globe

valves on the handwheel, $M = 1$) in the compression phase and for $K_p = 3.3 \times 10^5$ Pa s² (i.e., for a full valve-opening, $M = 0$) in the expansion phase of the hydraulic cylinder. Fig. 20 shows the comparison of the time series of W_{out} for $\gamma = 1.2$ and 3.3. The \bar{W}_{out} is lightly larger for $\gamma = 3.3$ ($\bar{W}_{out} = 37$ W and CWR = 26%) than for $\gamma = 1.2$ ($\bar{W}_{out} = 31$ W and CWR = 23%) due to the RAO and G_i show a limited variation, CWR shows a small dependence with variation of K_p and for higher value of γ the wave energy is concentrated over a smaller bandwidth.

The contour plot of CWR as a function of H_s and peak wave frequency, f_p , is shown in Fig. 21. The white line represents the maximum wave steepness, defined as $S_p = H_s/L_p$, where L_p is the peak wave length. The contours of CWR for both $\gamma = 1.2$ and 3.3 are very similar and, as expected, the CWR increases as H_s increases. The maximum CWR occurs firstly for $f_p \approx 0.42$ Hz, the same result was also obtained for regular waves (see Fig. 12a). For both γ , the CWR is greater than 28% across a broader bandwidth close to the

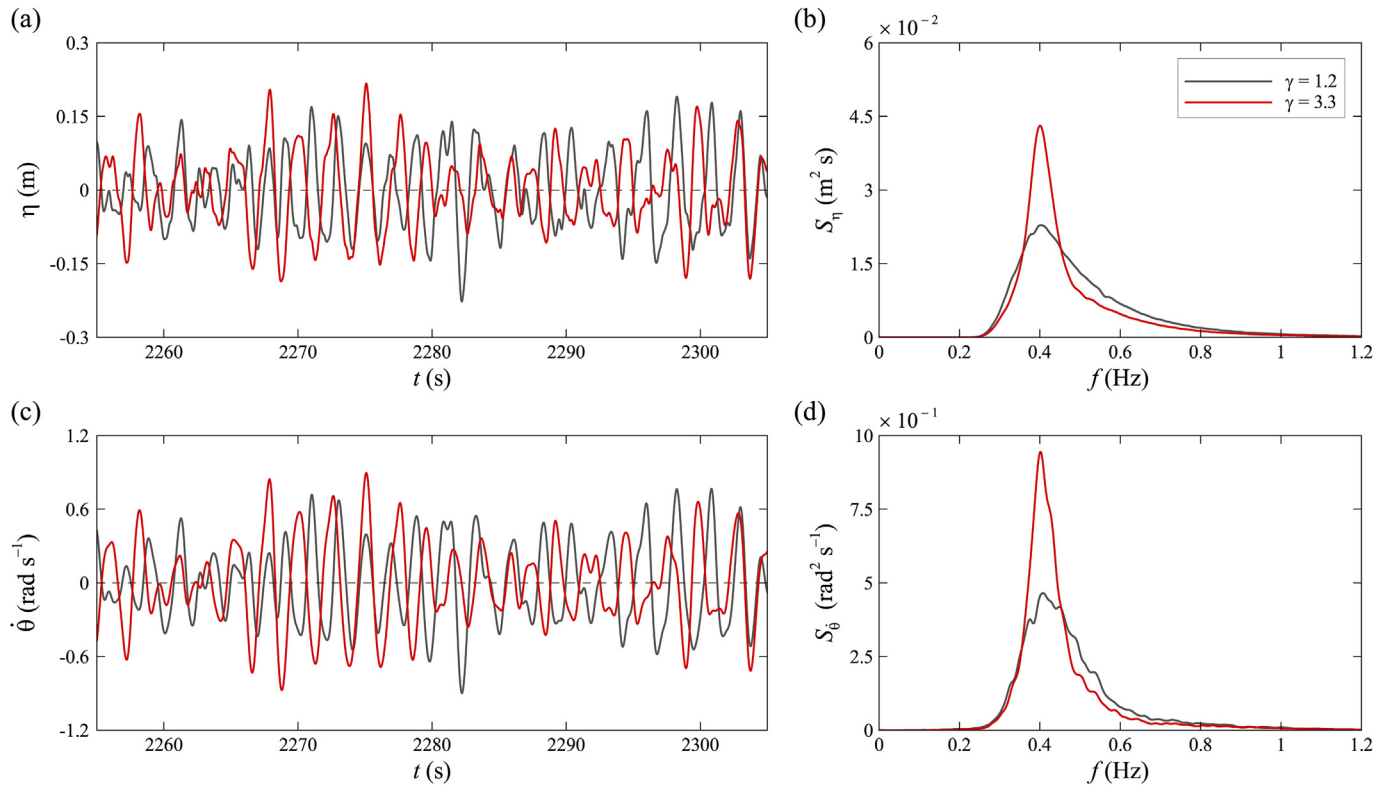


Fig. 19. Comparison of the computed data for $\gamma = 1.2$ and 3.3. Time series: (a) free-surface elevation; (c) angular velocity of the flap. Power spectra: (b) free-surface elevation; (d) angular velocity of the flap.

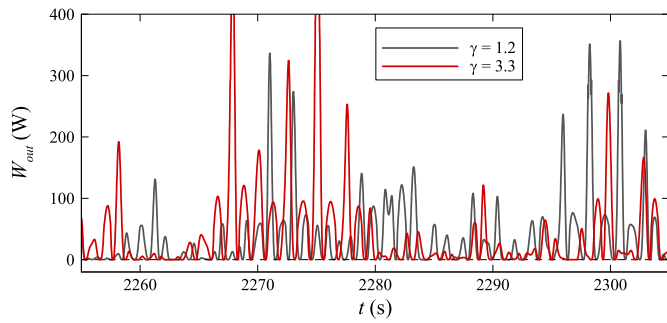


Fig. 20. Comparison of the time series of power capture for $\gamma = 1.2$ and 3.3.

maximum wave steepness.

6. Conclusions

In this paper the CWR and RAO of an OWSC with hydraulic PTO system are experimentally investigated. The experimental tests were performed for both unidirectional regular and irregular waves. The effects of PTO system and wave condition on the dynamics of an OWSC at 1:10 scale model were presented and analysed.

The preliminary results for regular waves indicate that the PTO system, wave frequency and height have a significant influence on the CWR and RAO. It was observed that the RAO decreases with increasing wave height, which may be due to the viscous dissipation caused by vortex shedding and wave nonlinearity that

increases with the increasing of wave height. However, the CWR does not seem to vary excessively with wave height, showing variation range less than 15%. Both CWR and RAO have a strong dependence on wave frequency. In general, a weak correlation between CWR and RAO was found, i.e., the maximum CWR about 21% does not occur for the maximum value of RAO. The hydraulic PTO system shows a strong nonlinear behavior, including cavitation phenomena for large amplitude of flap motion. The mathematical model of damping effect can predict the dynamic behaviors of the hydraulic PTO system with satisfactory accuracy.

The RAO curve of OWSC under irregular waves does not present a well-defined peak as from the linear theory, showing a limited variation in a broadband. It was observed that the RAO is strongly affected by the hydraulic PTO system. The time series of free-surface elevation, angular velocity of the flap and pressure in the PTO system are dominated by the linear component, however, they present some important higher-order frequency components. Therefore, to predict the variation of CWR with significant wave height and peak frequency, the nonlinear output frequency response functions were considered as the extension of the RAO to the nonlinear case. These functions also show a limited variation in a broad wave frequency band, presenting values of the same order of magnitude of RAO. It was observed that the CWR is strongly affected by the significant wave height and peak frequency. CWR greater than 28% was found for higher significant wave height close to the maximum wave steepness and therefore (for best results) the OWSC should be adjusted to match the sea state wave peak frequency.

The study shows that the inclusion of the hydraulic PTO system introduces nonlinear behaviors that affects the relation between

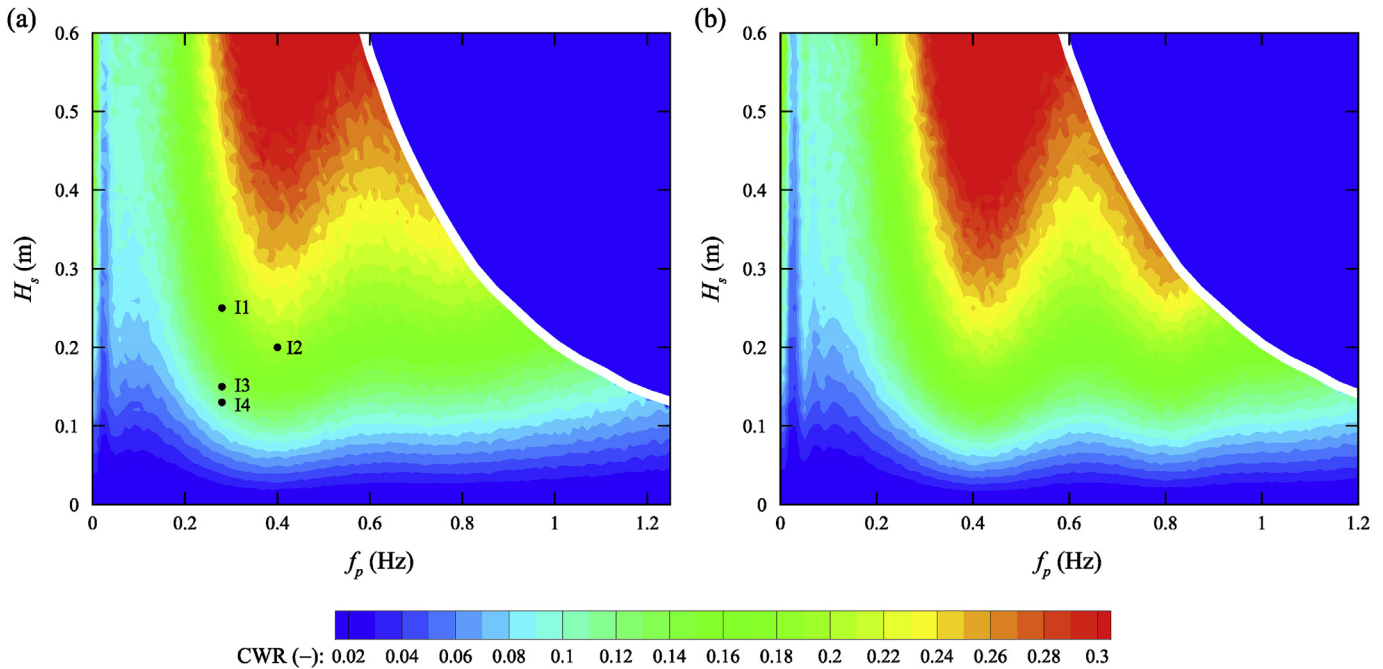


Fig. 21. Contour plot of CWR as a function of significant wave height and peak frequency for: (a) $\gamma = 1.2$; (b) $\gamma = 3.3$.

RAO and CWR, namely the maximum CWR may not be registered at peak RAO. This is an important result that has received limited attention. It has a significant impact on the design of the OWSC, call for further studies of particular flap and hydraulic PTO system pairs.

Declaration of competing interest

The authors declare that they have no known competing financial interests or personal relationships that could have appeared to influence the work reported in this paper.

Acknowledgments

The authors acknowledge IMFIA for allowing the realization of the experimental tests. This work was partially funded by FEDER, program COMPETE, and by national funds through Portuguese Foundation for Science and Technology (FCT) projects RECI/ECM-HID/0371/2012. The first author acknowledges the support of FCT through the Grant No. PD/BD/705970/2014.

Nomenclature

ΔX_1	variation of length of the measuring wire (m)
$\dot{\theta}$	angular velocity of the flap (rad s^{-1})
ε	random wave phase (rad)
η	free-surface elevation (m)
γ	peak enhancement (-)
λ	geometrical scale factor (-)
ω	angular frequency (rad s^{-1})
ρ	water density (kg m^{-3})
σ	Thoma coefficient (-)
θ	rotation angle of the flap (rad)
ε	mean reflected wave power ratio (-)
A	cross-section area of the cylinder chamber (m^2)
c_g	wave group velocity (m s^{-1})
f	wave frequency (Hz)
f_p	wave peak frequency (Hz)

g	gravitational acceleration (m s^{-2})
G_i	nonlinear output frequency response function ($\text{m}^2 \text{s}$)
H	wave height (m)
h	still water depth (m)
H_m	mean wave height (m)
H_s	significant wave height (m)
i	oscillation cycle number (-)
I_p	coefficient that takes into account the inertia of the fluid (Pa s^2)
$I_{xx}; I_{yy}; I_{zz}$	moment of inertia of the flap (kg m^2)
k	wave number (m^{-1})
K_p	coefficient of pressure loss (Pa s^2)
L	wave length (m)
L_p	peak wave length (m)
M	valve-opening (-)
m	mass of the flap (kg)
N	total number of wave cycles (-)
P_{atm}	atmosphere pressure (Pa)
P_c	water pressure inside the cylinder chamber (Pa)
P_v	vapor pressure of water (Pa)
S_η	power spectrum of the incident waves ($\text{m}^2 \text{s}$)
S_p	maximum wave steepness (-)
S_w	power spectrum of the wavemaker input signals ($\text{m}^2 \text{s}$)
T	wave period (s)
t	time (s)
T_p	wave peak period (s)
t_{total}	test duration (s)
W_i	period-average incident energy (W)
W_{out}	power capture (W)
$x_{12}; x_{23}$	distance between wave probes (m)

References

- [1] T. Whittaker, M. Folley, Nearshore oscillating wave surge converters and the development of oyster, *Philos. Trans. R. Soc. A Math. Phys. Eng. Sci.* 370 (2012) 345–364.
- [2] T. Whittaker, D. Collier, M. Folley, M. Osterried, A. Henry, M. Crowley, The development of Oyster – a shallow water surging wave energy converter, in: 7th Annual European Wave & Tidal Energy Conference, Portugal, Porto, 2007.

- [3] M. Folley, T. Whittaker, M. Osterried, The oscillating wave surge converter, in: The Fourteenth International Offshore and Polar Engineering Conference, International Society of Offshore and Polar Engineers, Toulon, France, 2004.
- [4] J. Lucas, M. Livingstone, N. Vuorinen, J. Cruz, Development of a wave energy converter (WEC) design tool - application to the waveroller wec including validation of numerical estimates, in: Fourth International Conference on Ocean Energy, Dublin, Ireland, 2012.
- [5] P. Schmitt, H. Asmuth, B. Elsaesser, Optimising power take-off of an oscillating wave surge converter using high fidelity numerical simulations, *Int. J. Mar. Energy* 16 (2016) 196–208.
- [6] N.F. Parsons, P.A. Martin, Scattering of water waves by submerged plates using hypersingular integral equations, *Appl. Ocean Res.* 14 (1992) 313–321.
- [7] N.F. Parsons, P.A. Martin, Scattering of water waves by submerged curved plates and by surface-piercing flat plates, *Appl. Ocean Res.* 16 (1994) 129–139.
- [8] N.F. Parsons, P.A. Martin, Trapping of water waves by submerged plates using hypersingular integral equations, *J. Fluid Mech.* 284 (1995) 359.
- [9] D. Evans, R. Porter, Hydrodynamic characteristics of a thin rolling plate in finite depth of water, *Appl. Ocean Res.* 18 (1996) 215–228.
- [10] E. Renzi, F. Dias, Resonant behaviour of an oscillating wave energy converter in a channel, *J. Fluid Mech.* 701 (2012) 482–510.
- [11] E. Renzi, F. Dias, Relations for a periodic array of flap-type wave energy converters, *Appl. Ocean Res.* 39 (2013b) 31–39.
- [12] E. Renzi, F. Dias, Hydrodynamics of the oscillating wave surge converter in the open ocean, *Eur. J. Mech. B Fluid* 41 (2013a) 1–10.
- [13] P. Schmitt, B. Elsaesser, On the use of OpenFOAM to model oscillating wave surge converters, *Ocean Eng.* 108 (2015) 98–104.
- [14] R. Gomes, M. Lopes, J. Henriquez, L. Gato, A. Falcao, The dynamics and power extraction of bottom-hinged plate wave energy converters in regular and irregular waves, *Ocean Eng.* 96 (2015) 86–99.
- [15] Y. Wei, A. Rafiee, A. Henry, F. Dias, Wave interaction with an oscillating wave surge converter. Part I: viscous effects, *Ocean Eng.* 104 (2015) 185–203.
- [16] Y. Wei, T. Abadie, A. Henry, F. Dias, Wave interaction with an oscillating wave surge converter. Part II: Slamming, *Ocean Eng.* 113 (2016) 319–334.
- [17] F. Dias, E. Renzi, S. Gallagher, D. Sarkar, Y. Wei, T. Abadie, C. Cummins, A. Rafiee, Analytical and computational modelling for wave energy systems: the example of oscillating wave surge converters, *Acta Mech. Sin.* 33 (2017) 647–662.
- [18] A. Henry, The Hydrodynamics of Small Seabed Mounted Bottom Hinged Wave Energy Converters in Shallow Water, Ph.D. thesis, Queen's University Belfast, 2009.
- [19] M. Folley, T. Whittaker, A. Henry, The effect of water depth on the performance of a small surging wave energy converter, *Ocean Eng.* 34 (2007) 1265–1274.
- [20] C.C. Lin, J.H. Chen, Y.C. Chow, S.Y. Tzang, S.J. Hou, F.Y. Wang, The experimental investigation of the influencing parameters of flap type wave energy converters, in: In 4th International Conference on Ocean Energy, Dublin, 2012.
- [21] P. Schmitt, S. Bourdier, D. Sarkar, E. Renzi, F. Dias, K. Doherty, T. Whittaker, J. van't Hoff, Hydrodynamic loading on a bottom hinged oscillating wave surge converter, in: Twenty-second International Offshore and Polar Engineering Conference, Rhodes, Greece, 2012.
- [22] A. Henry, O. Kimmoun, J. Nicholson, G. Dupont, Y. Wei, F. Dias, A two dimensional experimental investigation of slamming of an oscillating wave surge converter, in: The Twenty-fourth International Ocean and Polar Engineering Conference, Busan, Korea, 2014.
- [23] A. Henry, A. Rafiee, P. Schmitt, F. Dias, T. Whittaker, The characteristics of wave impacts on an oscillating wave surge converter, *J. Ocean Wind Energy* 1 (2014b) 101–110.
- [24] D. Ning, C. Liu, C. Zhang, M. Göteman, H. Zhao, B. Teng, Hydrodynamic performance of an oscillating wave surge converter in regular and irregular waves: an experimental study, *J. Mar. Sci. Technol.* 25 (2017) 520–530.
- [25] R. Alonso, S. Solari, L. Teixeira, Wave energy resource assessment in Uruguay, *Energy* 93 (2015) 683–696.
- [26] T.L. Andersen, P. Frigaard, Wave Generation in Physical Models: Technical Documentation for AwaSys 6, Department of Civil Engineering, Aalborg University, Denmark, 2014.
- [27] S. Hughes, *Physical Models and Laboratory Techniques in Coastal Engineering*, Advanced Series on Ocean Engineering, World Scientific, 1993.
- [28] W. Sheng, R. Alcorn, T. Lewis, Physical modelling of wave energy converters, *Ocean Eng.* 84 (2014) 29–36.
- [29] F. Floccard, T. Finnigan, Increasing power capture of a wave energy device by inertia adjustment, *Appl. Ocean Res.* 34 (2012) 126–134.
- [30] B. Méhauté, An Introduction to Hydrodynamics and Water Waves, Springer Berlin Heidelberg, 1976.
- [31] M. Brito, L. Teixeira, R.B. Canelas, R.M.L. Ferreira, M.G. Neves, Experimental and numerical studies of dynamic behaviors of a hydraulic power take-off cylinder using spectral representation method, *J. Tribol.* 140 (2017), 021102.
- [32] E. Mansard, E. Funke, The measurement of incident and reflected spectra using a least squares method, in: Coastal Engineering, American Society of Civil Engineers (ASCE), 1980.
- [33] A.J.N.A. Sarmento, Wave flume experiments on two-dimensional oscillating water column wave energy devices, *Exp. Fluid* 12 (1992) 286–292.
- [34] P. Stansby, E.C. Moreno, T. Stallard, A. Maggi, Three-float broad-band resonant line absorber with surge for wave energy conversion, *Renew. Energy* 78 (2015) 132–140.
- [35] J. Falnes, *Ocean Waves and Oscillating Systems: Linear Interactions Including Wave-Energy Extraction*, Cambridge University Press, Pitt Building, Trumpington Street, Cambridge, United Kingdom, 2002.
- [36] B.M. Count, D.V. Evans, The influence of projecting sidewalls on the hydrodynamic performance of wave-energy devices, *J. Fluid Mech.* 145 (1984) 361–376.
- [37] A. Henry, M. Folley, T. Whittaker, A conceptual model of the hydrodynamics of an oscillating wave surge converter, *Renew. Energy* 118 (2018) 965–972.
- [38] H. Santo, P.H. Taylor, E.C. Moreno, P. Stansby, R.E. Taylor, L. Sun, J. Zang, Extreme motion and response statistics for survival of the three-float wave energy converter M4 in intermediate water depth, *J. Fluid Mech.* 813 (2017) 175–204.
- [39] A.F. Falcao, Phase control through load control of oscillating-body wave energy converters with hydraulic PTO system, *Ocean Eng.* 35 (2008) 358–366.
- [40] A. Caska, T. Finnigan, Hydrodynamic characteristics of a cylindrical bottom-pivoted wave energy absorber, *Ocean Eng.* 35 (2008) 6–16.
- [41] Z.Q. Lang, S.A. Billings, Energy transfer properties of non-linear systems in the frequency domain, *Int. J. Control.* 78 (2005) 345–362.
- [42] D. Walker, P. Taylor, R.E. Taylor, The shape of large surface waves on the open sea and the draupner new year wave, *Appl. Ocean Res.* 26 (2004) 73–83.